Time-Resolved Whole-Brain CMRO2 Quantification by MR Susceptometry and Flow Mapping

Felix W Wehrli, Varsha Jain, Zachary Rodgers and Cheng Li
Laboratory for Structural NMR Imaging
Department of Radiology
University of Pennsylvania Perelman School of Medicine

Background/Purpose:
The cerebral metabolic rate of oxygen consumption (CMRO2) is a fundamental physiologic parameter that has only recently become amenable to measurement by noninvasive imaging modalities (*1*). Here, we present an approach based on simultaneous quantification of venous oxygen saturation (SvO2) and total flow, yielding CMRO2 in absolute physiologic units by invoking Fick's equation (*2*). We show that the method lends insight into the physiologic response to various stimuli.

Methods:
SvO2 is obtained by modeling the vein as a paramagnetic cylinder from which the induced field is obtained analytically by phase mapping relative to the surrounding tissue, typically in the superior sagittal sinus (SSS). Flow is quantified by phase-contrast imaging either from the major inflow conduits (internal carotid and vertebral arteries) or SSS that drains approximately 50% of total blood in the brain. Various embodiments are discussed in which flow and SvO2 are measured simultaneously, yielding CMRO2 with temporal resolutions as high 3 s, thereby permitting studies of non-steady state processes such as volitional apnea (*3*). Finally, in a translational project neurovascular reactivity in newborns with congenital heart disease was evaluated by subjecting the patients to transient hypercapnia (*4*).

Results:
Results obtained both experimentally and by forward calculation of the induced intravascular field in actual vascular geometries indicate that the analytical solution for an infinite cylinder is a robust approximation even in the case of significant deviations from circular cross-section, curvature and tapering. Baseline CMRO2 values in healthy subjects were found to agree with those obtained with established invasive techniques (*5*). Further, the response to hypercapnia – an isometabolic stimulus – did not affect CMRO2, as expected. In contrast, volitional apnea caused a transient increase in CMRO2 (*3*). The distinguishing behavior is likely due to apnea representing a non-steady state, mixed hypercapnic/hypoxic stimulus. Lastly, neonates with congenital heart disease, including hypoplastic left heart syndrome and transposition of the great arteries, in whom arterial blood is undersaturated, were found to respond normally to hypercapnia, i.e. increased flow commensurate with elevated SvO2 (*4*). Their baseline CMRO2, however, was lower by up to a factor of five relative to adults, likely as a result of the much lower oxygen demands of the undeveloped brain and the effect of sedation.

Conclusion:
MRI blood oximetry in conjunction with total flow measurement is a practical and robust method for evaluation of CMRO2 and a means to study neurovascular reactivity in patients.

References:
1. F. Xu, Y. Ge, H. Lu, Noninvasive quantification of whole-brain cerebral metabolic rate of oxygen (CMRO2) by MRI. *Magn Reson Med* **62**, 141 (2009).
2. V. Jain, M. C. Langham, F. W. Wehrli, MRI estimation of global brain oxygen consumption rate. *Journal of cerebral blood flow and metabolism* **30**, 1598 (Sep, 2010).
3. Z. Rodgers, V. Jain, M. C. Langham, F. W. Wehrli, in *20th Annual ISMRM Scientific Meeting*. (ISMRM, Melbourne, Australia, 2012), 461.
4. V. Jain *et al.*, in *21st Annual ISMRM Scientific Meeting*. (ISMRM, Salt Lake City, Utah, 2013), in press.
5. V. Jain *et al.*, Rapid magnetic resonance measurement of global cerebral metabolic rate of oxygen consumption in humans during rest and hypercapnia. *Journal of cerebral blood flow and metabolism* **31**, 1504 (2011).

Iron and Neurological Diseases

James R. Connor, Ph.D.
Department of Neurosurgery
Penn State Hershey Medical Center

Background/Purpose:

A number of devastating neurological disorders are associated with either too much or too little iron in the brain. For example, excessive brain iron accumulation is reported in Parkinson's and Alzheimer's Diseases, amyotrophic lateral sclerosis, neurodegeneration with brain iron accumulation and Huntington's Disease. On the other hand, iron deficiency remains the most prevalent micronutrient problem in the world and it is known that too little brain iron during development results in significant cognitive and performance deficits reflecting impairments in myelination and neurotransmitter production. Brain iron deficiency during adulthood also appears to underlie the pathobiology of a common neurological disorder known as Restless Legs Syndrome. Although brain iron concentrations are currently considered static, the maintenance of brain iron homeostasis appears much more dynamic than previously thought, particularly given a recent report of cyclical day/night variation in brain iron levels. In addition, genetics also play a role in brain iron levels as has been shown in both in-bred strains of mice and humans. In humans, both HFE gene variants (the most common polymorphism in Caucasians) as variants of the transferrin gene are associated with differences in brain iron status and those changes in brain iron concentrations are associated with cognitive performance. Moreover, mutations in the HFE protein are associated with a four-fold increase in risk of amyotrophic lateral sclerosis. Thus, elucidation of the mechanism(s) by which the brain acquires iron and, equally important, the regulation of brain iron transport, can provide insights into the adaptive responses involved in maintaining brain iron homeostasis and those that contribute to the maladaptive responses emergent with neurobiological disease.

Conclusion:

In this talk we will review the data on changes in brain iron with aging and disease and discuss novel animal models in which to interrogate brain iron status.

References:

1. Leitner DF, Connor JR. Functional roles of Transferrin in the Brain. Accepted for publication *to Biochimica et Biophysica Acta*, 2011.

2. Todorich B, Pasquini J, Garcia C, Paez P, Connor JR: Oligodendrocytes and myelination: the role of iron. *GLIA* 57(5):467-478, 2009.

3. Nandar W, Connor JR. HFE Gene Variants Affect Iron in the Brain. *The Journal of Nutrition*. 141:729S-739S, 2011.

Computational Methods for Inverse Problems

James G. Nagy[1]
[1]*Mathematics and Computer Science Department, Emory University, Atlanta, GA, 30322, USA*

Background/Purpose:

Inverse problems arise in many medical imaging applications, such as image reconstruction. Such problems are sensitive to noise in the measured data. Many algorithms have been developed to compute approximate solutions of inverse problems, but they may differ in a variety of ways. For example, there are several different regularization methods one could use, and for each of these, various methods for choosing regularization parameters. These choices may depend on statistical assumptions imposed on the forward model and the noise. To use algorithms effectively, it is essential to understand how they perform on a variety of problems.

Methods:

We describe some basic approaches to solving inverse problems, such as filtering and iterative methods. We discuss various regularization schemes that can be used, and the tradeoffs one must consider. The theory of linear problems is much more developed than it is for nonlinear problems. This is due, in large part, to the fact that the numerical treatment of nonlinear inverse problems is often highly dependent on the particular application. However, good intuition can be gained by studying linear inverse problems, which can be then used to develop approaches for nonlinear inverse problems.

Results:

Properties of algorithms discussed in this talk will be illustrated by several numerical examples. We show that with proper choices of parameters, the algorithms can compute accurate reconstructions. In addition, we show that incorporating nonlinear physics into the mathematical model can allow for much better image reconstructions than using simplifying approaches. We illustrate this, in particular, for tomosynthesis imaging, where a nonlinear iterative approach produces much better reconstructed images than a standard filtered back-projection method.

Conclusion:

The discussion and examples used in this talk illustrate the range of difficulties that can be encountered when solving inverse problems, and we discuss the issues that must be addressed when designing algorithms.

References:

1. J. Chung, S. Knepper, J. G. Nagy. *Large-Scale Inverse Problems in Imaging*, Chapter 2 in Handbook of Mathematical Methods in Imaging, Otmar Scherzer, ed., Springer, (2011), pp. 43-86.

2. P. C. Hansen, J. G. Nagy, D. P. O'Leary. *Deblurring Images: Matrices, Spectra and Filtering*, SIAM Press, Philadelphia, 2006.

3. J. Chung, J. G. Nagy, I. Sechopoulos. *Numerical Methods for Polyenergetic Digital Breast Tomosynthesis*, SIAM J. Imaging Sci., 3 (2010), pp. 133-152.

4. H. W. Engl, M. Hanke, A. Neubauer. *Regularization of Inverse Problems,* Kluwer Academic Publishers, Dordrecht, 2000.

5. P. C. Hansen. *Discrete Inverse Problems: Insight and Algorithms,* SIAM Press, Philadelphia, 2010.

6. J. L. Mueller, S. Siltanen. *Linear and Nonlinear Inverse Problems with Practical Applications,* SIAM Press, Philadelphia, 2012.

Susceptibility manifestation of Multiple Sclerosis

Susan A. Gauthier*, DO, MPH, Weiwei Chen, MD, PhD, Ajay Gupta, MD, Joseph Comunale, MD, Tian Liu, PhD, Shuai Wang, MS, Mengchao Pei, MS, Yi Wang, PHD

Radiology and Neurology*, Weill Medical College of Cornell University, New York, USA

PURPOSE & METHODS: Multiple sclerosis (MS) MS is a chronic inflammatory disease of central nervous system characterized by focal T cell and macrophage/microglia infiltrates associated with demyelination. In the majority of patients, MS begins as a relapsing-remitting course but eventually evolves to a state of progressive decline in disability. Focal inflammatory demyelinating lesions are the predominant pathological findings in the patients with relapsing disease whereas diffuse axonal injury with microglial activation has been found to be the hallmark of progressive disease.[1] Microglial activation itself occurs either as a response to CNS injury for example as in Wallerian degeneration, or in response to signals from other inflammatory cells including macrophages and lymphocytes. Further understanding the role of the innate immune system in MS, especially in progressive disease, will further our potential to translate new therapies. Imaging biomarkers to measure microglia activity is currently an unmet need within the field. Pathological studies have indicated that some populations of activated macrophages/microglia are cellular sources of iron[2], for this reason utilizing MRI to image iron may potentially be a new biomarker for the disease. Paramagnetic iron causes an increase in tissue susceptibility, which can be detected in MRI [3,4,5] and quantitative susceptibility mapping (QSM) enables a direct measure of tissue susceptibility. We utilized QSM to assess the level and temporal change of susceptibility among MS lesions at various ages.

RESULTS: Thirty-two clinically confirmed MS patients underwent MRI, which included a 3D multiecho GRE sequence with QSM reconstruction. To estimate the ages of MS lesions, all available prior MRIs (performed 0.3 – 10.6 years ago) were examined. Lesion susceptibilities relative to normal appearing white matter (NAWM) and temporal rate of change were obtained from QSM images. We found 162 MS lesions being age measurable due to the availability of prior scans. The relative susceptibility on average was .5, 35, 42, -2, 1, and .6 ppb (part per billion) for early enhancing lesions (0y), early non-enhancing lesions (0 – 2y), lesions aged 2 – 4y (no lesions aged 4– 6y), 6 – 8y, 8 – 10y, and > 10y, respectively. The most rapid short-term susceptibility increase was found among lesions transitioning from enhancing to non-enhancing.

CONCLUSIONS: Magnetic susceptibility increases rapidly as lesions change from enhancing to non-enhancing, plateaus and gradually dissipates as lesions age. These susceptibility changes may reflect the changing pathophysiological mechanisms within the lesions. Our results suggest that the inflammatory cells present at the earliest stages of lesion development are not iron rich. However, the observed rapid increase in susceptibility is suggestive that iron accumulates rapidly in lesions after loss of gadolinium enhancement. If the high paramagnetic susceptibility measured in QSM is to be interpreted as iron acquired by microglia/macrophages, this observation is suggestive of a transition to a different subpopulation of cells. However, phenotypic identification of the specific subpopulations of macrophages/microglia that have a propensity to contain iron and their role in the pathogenesis of MS remains poorly understood. Future studies are warranted to understand the underlying cellular processes of MS lesion susceptibility change and the pathological significance of these cellular changes.

REFERENCES:

1. Kutzelnigg A, Lucchinetti CF, Stadelmann C, et al. Cortical demyelination and diffuse white matter injury in multiple sclerosis. Brain 2005;128:2705-12.
2. Bagnato F, Hametner S, Yao B, et al. Tracking iron in multiple sclerosis: a combined imaging and histopathological study at 7 Tesla. Brain 2011;134:3602-3615.
3. Haacke EM, Makki M, Ge Y, et al. Characterizing iron deposition in multiple sclerosis lesions using susceptibility weighted imaging. J Magn Reson Imaging 2009;29:537-544.
4. Khalil M, Teunissen C, Langkammer C. Iron and neurodegeneration in multiple sclerosis. Mult Scler Int 2011;2011:606807.
5. Ropele S, de Graaf W, Khalil M, et al. MRI assessment of iron deposition in multiple sclerosis. J Magn Reson Imaging 2011;34:13-21.

Large-Scale Inverse Problems in Imaging

Julianne Chung[1]
[1]*Mathematics Department, Virginia Tech, Blacksburg, VA 24061, USA*

Background/Purpose:

Many scientific and engineering applications require numerical methods to compute efficient and reliable solutions to inverse problems. Inverse problems arise in important applications, including biomedical imaging, geophysics, astrophysics, inverse scattering and molecular biology; see for example, [1,3,4,5] and the references therein. Oftentimes, real-life applications require the computer to process extremely large amounts of data, and previously proposed methods for solving inverse problems are not adequate for these large-scale problems. The focus of our work is to develop numerical methods that can efficiently and accurately solve large-scale inverse problems.

Methods:

In order to obtain meaningful reconstructions, regularization is needed to stabilize the inversion process. Typically, this is done by imposing prior knowledge regarding the noise in the data and prior knowledge regarding the unknown solution. In this talk, we describe a framework that uses data from calibration experiments to pre-compute optimal spectral filters that are used for obtaining reconstructions. We formulate the problem in an empirical Bayes risk minimization framework in order to incorporate statistical information, and we use efficient methods from stochastic and numerical optimization to compute optimal filters. Our formulation of the optimal filter problem is general enough to use a variety of assessments of goodness of the solution estimate, and the computational methods are efficient for large-scale problems [2].

Results:

Numerical examples from image deconvolution illustrate that our proposed filters perform consistently better than well-established filtering methods. Furthermore, we show how our approach leads to easily computed uncertainty estimates for the pixel values.

Conclusion:

Large-scale inverse problems continue to be a thriving research interest in the mathematics, computer science, and image processing communities. In particular, reconstructing susceptibilities from measured magnetic field is a large-scale ill-posed inverse problem [6], and methods developed here can be extended to QSM applications.

References:

1. M. Bertero and P. Boccacci. *Introduction to Inverse Problems in Imaging*. Institute of Physics Publishing, Bristol, 1998.
2. J. Chung, M. Chung, and D. P. O'Leary. *Designing Optimal Spectral Filters for Inverse Problems.* SIAM J Scientific Computing, 33 (2011), 3132-3152.
3. J. Chung, S. Knepper, J. G. Nagy. *Large-Scale Inverse Problems in Imaging*, Chapter 2 in Handbook of Mathematical Methods in Imaging, Otmar Scherzer, ed., Springer, (2011), pp.43-86
4. J. L. Mueller, S. Siltanen. *Linear and Nonlinear Inverse Problems with Practical Applications,* SIAM Press, Philadelphia, 2012.
5. J. Kaipio and E. Somersalo. *Statistical and Computational Inverse Problems*. Springer, New York, 2005.
6. L. de Rochefort, T. Liu, B. Kressler, J. Liu, P. Spincemaille, V. Lebon, J. Wu, and Y. Wang. *Quantitative Susceptibility Map Reconstruction from MR Phase Data Using Bayesian Regularization: Validation and Application to Brain Imaging.* Magnetic Resonance in Medicine, 63 (2010), 194-206.

Cellular and animal models potentially useful for testing the new imaging technology and some relevant findings with the cellular models

Michael D Garrick[1]
[1]*University at Buffalo, Buffalo, NY 14214*

Background/Purpose: The new imaging technology that is the focus of this conference should soon allow improvements in subcellular imaging as well as enhancements for imaging tissues and specific anatomy in medical and biological studies. This presentation will cover cell lines where the investigator can manipulate intracellular levels of anyone of several metals chosen and mutant rodents where the levels of iron in particular can be altered compared to normal. The intent is to help attendees find appropriate models to test the capabilities under development.

Animal models: The 1st animal model is the Belgrade rat. This rat has a severe anemia inherited as an autosomal recessive. The genetic defect is a missense mutation (G185R) in divalent metal (ion) transporter (DMT1), a proton-coupled transporter of multiple metal ions [1]. The most important substrate physiologically is Fe^{2+}, but other metals such as Mn^{2+} are also transported. DMT1 is the major GI importer of iron, and also exports iron from endosomal vesicles during the transferrin cycle. DMT1 almost certainly has other roles in iron homeostasis. The Belgrade rat is therefore a model for iron deficiency and has successfully been used to show that R2* mapping will detect the regions of diminished brain iron in the mutant [2]. Remarkably, the animal model can also be induced into local iron overload as well [3, 4].

The thalassemic mouse is an animal model that spontaneously accumulates iron in multiple tissues [5] resembling the human disorder thalassemia intermedia. Homozygous deletion of the ß major globin gene leaves the synthesis of adult hemoglobin dependent on only the ß minor globin gene and the α globin gene. The imbalance in globin synthesis leads to anemia and iron overload. Subsequently other mouse models for thalassemia have been generated; these too develop iron overload.

Genetic engineering technology has allowed investigators to create other animal models that develop iron overload in multiple tissues [6]. The mouse gene for DMT1 has been manipulated so that one can develop tissue specific ablation (the cre–lox system) to see where its expression is critical for iron uptake [7].

Cellular models: We created 2 cell lines that overexpress 1 of 2 isoforms of DMT1 in a regulated fashion [8]. These lines provide the opportunity to manipulate intracellular levels of iron (or Mn) by increasing import. We will describe some of the things that one can do with such cells. Of particular interest, we have just used these cells as part of a study showing that DMT1 is a potential iron importer for mitochondria, the subcellular site where half or more iron flux within cells occurs [8].

References:

1. Fleming, M.D., et al., *Nramp2 is mutated in the anemic Belgrade (b) rat: Evidence of a role for Nramp2 in endosomal iron transport.* Proc. Natl. Acad. Sci. USA, 1998. **95**(3): p. 1148-1153.
2. Zywicke, H.A., et al., *Microscopic R2* mapping of reduced brain iron in the Belgrade rat.* Ann. Neurol., 2002. **52**(1): p. 102-105.
3. Garrick, M., et al., *Iron supplementation moderates but does not cure the Belgrade anemia.* BioMetals, 1997. **10**: p. 65-76.
4. Thompson, K., et al., *Belgrade Rats Display Liver Iron Loading.* The Journal of Nutrition, 2006. **136**(12): p. 3010-3014.
5. Garrick, L.M., et al., *Tissue Iron Deposition in Untransfused Beta Thalassemic Mice.* Exp. Hematol., 1989. **17**: p. 423-428.
6. Levy, J.E., et al., *The C282Y mutation causing hereditary hemochromatosis does not produce a null allele.* Blood, 1999. **94**(1): p. 9-11.
7. Gunshin, H., et al., *Slc11a2 is required for intestinal iron absorption and erythropoiesis but dispensable in placenta and liver.* The Journal of Clinical Investigation, 2005. **115**(5): p. 1258-1266.
8. Garrick, M.D., et al., *Comparison of mammalian cell lines expressing distinct isoforms of divalent metal transporter 1 in a tetracycline-regulated fashion.* Biochem J, 2006. **398**(3): p. 539-546.

Basic steps for doing Quantitative Susceptibility Mapping (QSM)

Tian Liu, PhD[1]
[1]*Radiology, Weill Cornell Medical College*

Background/Purpose:

Quantitative susceptibility mapping (QSM) provides a new kind of imaging biomarker to investigate physiological status and pathological changes. It is useful for chemical identification and quantification of specific substances including iron, calcium, gadolinium, and super paramagnetic iron oxide (SPIO) nano-particles. Calculation of susceptibility from MRI phase data involves solving a series of inverse problems that are technically stimulating, and there have been increased number of methods that aim to solve this problem. In this manuscript, a framework is provided for the QSM reconstruction.

Signal Model:

In QSM, it is assumed that a spatially varying susceptibility distribution inside a given region of interest (ROI) induces a local inhomogeneous magnetic field. This local field is further superimposed by a background magnetic field that is caused by other susceptibility sources outside the ROI. Finally, the total field inhomogeneity is reflected in the phase image acquired using a gradient echo sequence (Fig. 1). Therefore, there are essentially three challenges needed to be overcome to obtain a QSM: 1) estimate the field inhomogeneity, 2) remove the background field contribution, 3) invert the dipole fields.

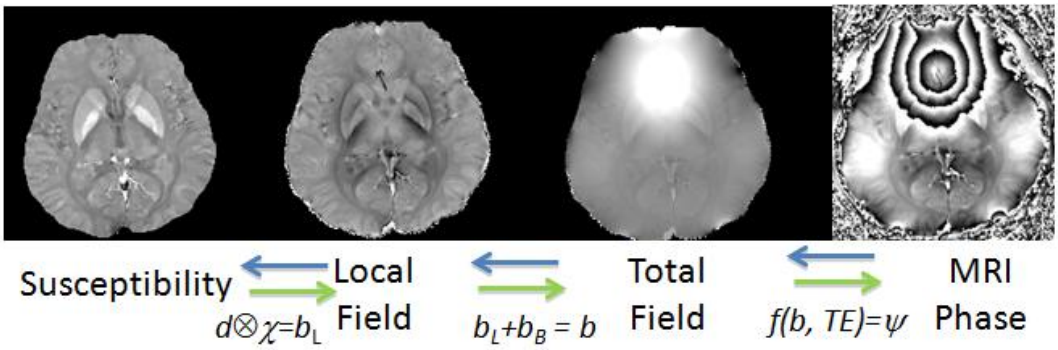

Basic steps for doing QSM

1) Field map estimation: Both single-echo[1] and multi-echo[2] acquisitions have been applied to estimate field map. In both methods, the phase is formulated as a linear function of the magnetic field. Repetitive experiments have shown that this simple relationship provides a reliable estimation when chemical shift and flow induced shift are absent. In the presence of chemical shift, water/fat separation algorithms need to be employed. Flow compensated sequence with adaptive quadratic fitting enables reliable measurements in vessels[3]. Phase unwrapping are also often encountered to overcome frequency aliasing caused by large off-resonance frequency and long TE spacing.

2) Background field removal: Two strategies exist, implicit methods where background field removal is incorporated with dipole inversion[4], or explicit methods where background field is removed prior to dipole inversion. Most literature adopts the explicit method. Fundamentally, background field estimation is classical problem in magnetostatics, in the sense that a solution to the Laplace's equation with certain boundary conditions is sought-after. This solution could be found by searching for a linear combination of the basis functions to Laplace's equation, which is essentially the Projection onto Dipole Fields (PDF)[5] method, or by performing an inverse Laplacian, which is essentially the Sophisticated Harmonic Artifact Reduction on Phase data (SHARP)[6].

3) Dipole inversion: COSMOS[7,8] is a physical method that does not rely on prior information but requires sampling the same object from at least three different orientations. Various regularization methods have been proposed for single-orientation quantitative susceptibility mapping (QSM), which is an ill-posed magnetic field to susceptibility source inverse problem. Noise amplification, a major issue in inverse problems, manifests as streaking artifacts and quantification errors in QSM. These methods may be split into two categories, non-Bayesian methods[9, 10, 11] where the inversion is primarily formulated in Fourier domain that allows fast calculation, or Bayesian methods[1,12,13] where the inversion is formulated in image domain to allow incorporation of noise weighting. More freedom on the choice of prior is also provided using the Bayesian formulation.

Conclusion:

A frame work is provided in this work for setting up the inversion process from MRI phase data to quantitative susceptibility maps. QSM is a challenging engineering problem that invites further investigation.

References:

1. Bilgic et al, NeuroImage:59(3):2625-35; 2. de Rochefort et al, MRM:63(1):194-206; 3. Xu et al, ISMRM 13pp0165; 4. Schweser et al, MRM2012; 5. Liu et al, NMR Biomed:24(9):1129-36; 6 Schweser et al, Neuroimage:54(4):2789-8077; 7. Liu et al, MRM:61(1):196-204;8. Wharton et al, MRM:63(5):1292-304;9. Shmueli et al, MRM:62(6):1510-22; 10. Li et al, Neuroimage:55(4):1645-56; 11. Tang et al, MRM2012; 12. Liu et al, MRM:66(3):777-83. 13. Schweser et al, Neuroimage:62(3):2083-100

Phase processing for Quantitative Susceptibility Mapping (QSM)

Ferdinand Schweser
Medical Physics Group, IDIR I, Jena University Hospital - Friedrich Schiller University Jena, Germany,

Quantitative Susceptibility Mapping (QSM) aims to determine from an observed magnetic field perturbation $\Delta B = B - B_0$ the underlying susceptibility distribution χ that produces the perturbation, or in other words, to solve the inverse field-to-source problem

$$\Delta B(\vec{r}) = B_0 \int_{r \neq r'} \mathrm{d}^3\vec{r}'\chi(\vec{r}')d_z(\vec{r} - \vec{r}')$$

where d_z is the z-component of the spatial unit dipole response, B_0 is the strength of the applied magnetic field, and B is the total (perturbed) magnetic field [1].

The most established technique for assessing noninvasively the magnetic field perturbation in biological tissue is gradient-echo (GRE) MRI with relatively long echo times (TE). The phase φ of complex-valued GRE images reflects the Larmor frequency distribution

$$f_L = -\gamma \cdot B / 2\pi$$

and, thus, indirectly the magnetic field perturbation (right-handed MR system):

$$\varphi = \varphi^0 + 2\pi \cdot (f_L - f_0) \cdot TE = \varphi^0 - \gamma \cdot \Delta B \cdot TE,$$

where f_0 is the adjusted reference (demodulation) frequency, φ^0 is the signal phase at TE = 0 ms, and γ is the gyromagnetic ratio.

The objective of this talk is to provide an overview of the processing steps that need to be applied to raw GRE phase data before QSM can be performed. In the most general case GRE data are acquired using a multi-channel receive array with N_c coils and N_e echoes at different echo times resulting in $N_c \times N_e$ phase images. *Phase image reconstruction* from the individual coil images and *field mapping* extract the total (physical) magnetic field perturbation, ΔB, from the raw phase measurements, φ. Then, field contributions originating from susceptibility variations outside of the region of interest need to be eliminated. Figure 1 schematically illustrates the phase processing steps.

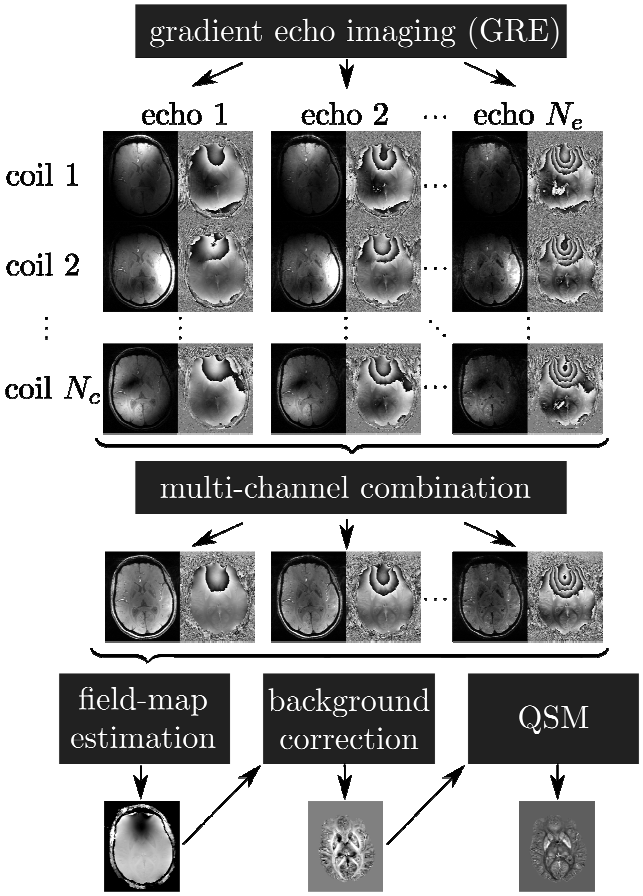

FIGURE 1. Schematic illustration of phase processing for QSM.

References

[1] J. P. Marques and R. W. Bowtell, *Concepts Magn Reson B Magn Reson Eng*, 25B(1):65–78, 2005.

Magnetic Susceptibility of Brain White Matter

Chunlei Liu[1, 2]
[1]*Brain Imaging and Analysis Center,* [2]*Department of Radiology, Duke University, Durham, NC, USA*

Background:

White matter occupies roughly half the volume of an adult human brain. It consists largely of glial cells and myelinated axons. While traditionally thought of a passive signal transmission unit, white matter has recently been shown to actively participate in learning and brain functions. Abnormalities in white matter have been implicated in a wide range of neurological disorders and diseases including, for example, multiple sclerosis, mental disorders and traumatic brain injuries. Changes in the cellular and molecular composition of the white matter result in changes in its magnetic properties. Imaging magnetic susceptibility with MRI thus offers a novel method to study the microstructure of white matter and may provide a new way to diagnose and characterize white matter diseases.

Methods:

Magnetic susceptibility can be measured with a 3D gradient-echo MRI sequence (1-3). This sequence generates a complex image that includes both magnitude and phase. From the phase images, magnetic susceptibility is calculated by solving a deconvolution problem *via* the technique of quantitative susceptibility mapping (QSM) (4-6). Two quantities can be derived as a measure of magnetic susceptibility: the apparent magnetic susceptibility and the anisotropic susceptibility tensor (7). Apparent magnetic susceptibility reflects the voxel-averaged bulk magnetization induced by a magnetic field applied in a given direction. Susceptibility tensor, on the other hand, measures the orientation dependence of the magnetization. The relationship between magnetic susceptibility and the molecular composition and cellular architecture of white matter have been investigated by theoretical analysis, simulation and animal models.

Results:

1. Myelin There are growing evidences supporting that the diamagnetic susceptibility of white matter predominately originates from the myelin sheath that insulates the axons. When the myelin is depleted, white matter becomes less diamagnetic and the susceptibility contrast between gray and white matter nearly vanishes. This has been demonstrated in the shiverer mice (8), cuprizone treated mice (9) and neonatal mice (10). The transgenic shiverer is an autosomal recessive mutation characterized by an almost total lack of myelin in the central nervous system, resulting in a near loss of susceptibility contrast (Fig. 1). In neonatal mice, on the other hand, myelin has not fully developed. These studies together demonstrate myelin as the main source of diamagnetic susceptibility in the white matter.

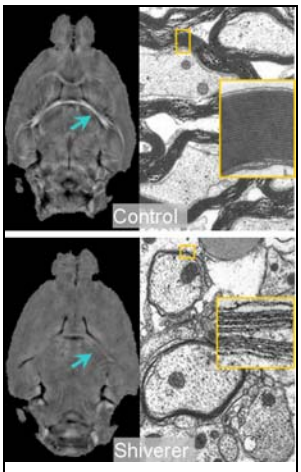

Fig. 1. Susceptibility shows high contrast in control mice which have thick myelin sheath (EM on the right); the contrast disappears in the shiverer which lacks myelin.

2. Axon Axon provides the structural support for an ordered arrangement of spiraling sheaths of myelin lipid bilayers. Each lipid molecule exhibits an anisotropic magnetic susceptibility. The long axis of a lipid molecule (mostly phospholipids) is arranged radially surrounding the axons. In brain white matter fiber bundles, these axons are roughly parallel to each other. Because of this highly structured organization, the bulk susceptibility measured over a voxel still exhibits orientation dependence (11). When the axons are parallel to the applied field, the measured susceptibility will be most paramagnetic. This anisotropic property can be described a tensor.

3. Compartmentalization The lipid bilayers are tightly packed structures with hydrophobic tails pointing towards the interiors of the bilayer. Consequently, the myelin sheath has low permeability for water molecules, resulting in compartmentalized structure in the white matter: axonal space, myelin and extracellular space. These three compartments have distinctive relaxation and magnetic properties. This compartmentalization can be probed by a variety of methods including varying sequence parameters (TE, TR and flip angle), applying saturation, introducing contrast agent or imaging non-proton nuclei (12). As one example, this compartmentalization introduces noneponential T2* decay (13).

Conclusion:

Imaging magnetic susceptibility provides a new tool to study the structure and function of brain white matter. It complements other existing MRI techniques such as diffusion MRI, mutli-compartment T1/T2 analysis and magnetization transfer measurement. A unique advantage of magnetic susceptibility for imaging the brain is its high efficiency, the superior spatial resolution and low specific absorption rate. It thus may help overcome certain limitations in existing methods at 3T and especially at ultra-high fields.

References: 1. Haacke, E.M. et al, MRM 2004; 52:612-618. **2**. Rauscher, A. et al, AJNR 2005; 26:736-742. **3**. Duyn, J.H. et al, PNAS 2007; 104:11796-11801. **4**. Shmueli, K. et al, MRM 2009; 62:1510-1522. **5**. de Rochefort, L. et al, MRM 2010; 63:194-206. **6**. Li, W. et al, NeuroImage 2011; 55: 1645-1656. **7**. Liu, C. MRM 2010; 63:1471-1477. **8**. Liu, C. et al, NeuroImage 2011 ; 56 :930-938. **9**. Lee, J. et al, NeuroImage 2012; 59:3967-3975. **10**. Argyridis, I. et al, Proc of 20th ISMRM, 2012; 410. **11**. Li, W. et al, NeuroImage 2012; 59: 2088-2097. **12**. Liu, C. et al, Proc of 20th ISMRM, 2012; 417. **13**. van Gelderen, P. et al, MRM 2012; 67: 110-117.

Quantitative Susceptibility Mapping inversion algorithms: image space based approaches

Ludovic de Rochefort[1]
[1]*Univ. Paris-Sud, CNRS IR4M UMR8081, Orsay, France*

Purpose:

The quantitative mapping of magnetic susceptibility using MRI (QSM) provides an additional tool that may benefit many clinical applications involving iron, paramagnetic and superparamagnetic contrast agents or diamagnetic calcifications. QSM corresponds to the reconstruction of a susceptibility map consistent with the field extracted from phase images. Many algorithms and constraints have been proposed in the past years based on k-space and image space inverse filtering[1-5]. This presentation will cover the types of spatial constraints practically encountered. Whenever non-uniform effects need to be considered or imposed in image space (field masking, internal source extraction, piece-wise smoothing, etc…), iterative algorithms provides a convenient way to perform reconstruction. We will limit to expressing reconstruction as a linear least-squares (LS) minimization and discuss the implementation of the conjugate gradients (CG) algorithm to solve it.

Methods:

From the approximation of magnetostatic equations, a linear relationship between the field B_z along B_0 and the susceptibility X can be expressed as a 2nd order filter in frequency domain[6]: $k^2\mathrm{FT}(B_z)=\mathrm{B}_0(k^2/3-k_z^2)\mathrm{FT}(X)$, where FT denotes the Fourier transform. The reconstruction of susceptibility from field is ill-posed as close to $k^2/3-k_z^2=0$, imprecise measures of B_z frequencies are obtained. Additionally, in image regions with limited SNR, B_z is poorly determined constituting a 1st spatial constraint (Fig.1a). In phase-based measurements, the precision can be assumed to be proportional to magnitude[7] W, and spatial weighting for B_z needs to be considered (Fig.1b). Secondly, highlighting differences between tissues inside a region-of-interest (ROI) is usually sought requiring removing external source contribution. It constitutes a 2nd type of spatial constraint (Fig.1c,d). Finally, piece-wise constant or smooth regions may be imposed to further enhance the reconstruction (Fig.1e). The LS minimization: $\min_X||W(B_0\mathrm{D}X-B_z)||^2+\alpha||\mathrm{L}X||^2$ exemplify how spatial constraints can be accounted for. D denotes the linear operator from susceptibility to field; L is a linear operator encompassing the constraints and α, the associated regularization parameter. To perform the reconstruction, the CG algorithm[8] can be used, avoiding forming the large matrices involved. Visual criteria and residual norm considerations[4] provide methods for choosing α (Fig.f and g).

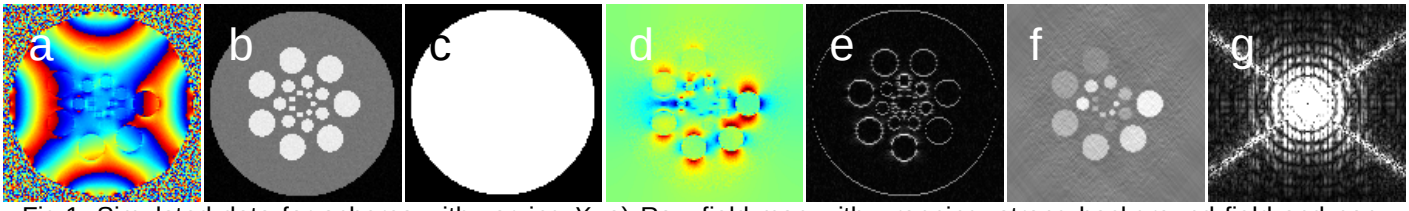

Fig.1: Simulated data for spheres with varying X. a) Raw field map with wrapping, strong background field and non-uniform noise. b) Associated magnitude image W providing a measure of precision on field. c) ROI in which internal effects (d) are extracted. e) Example of a spatial prior to perform piece-wise smoothing: the gradient of X is forced to be 0 at selected locations. f) Example of reconstructed X map and associated k-space (g) displaying noise propagation close to the magic angle and indicating a non-optimal α.

Results/discussion:

The limited information available on the measured field B_z, both in image space and k-space, has to be accounted for in the reconstruction. The addition of spatial priors on X enhances the various reconstruction steps, from the extraction of internal effects to final susceptibility maps[4]. The approach is flexible in the definition of priors and the resolution with the CG algorithm is simple to implement. Reconstruction duration can be reduced through pre-conditioning with faster technique[1] providing a starting point for the CG algorithm and through efficient search techniques for the regularization parameter α. However, spatial priors require an adequate definition[2], which indicates that QSM reconstruction will gain accuracy if combined with an enhanced segmentation. These inversion principles can be extended to image-based priors involving other than quadratic norms favoring properties (e.g sparsity) that may be adequate in given situations[9].

References: [1]Schmueli et al., MRM 2009. [2]Wharton et al., Neuroimage 2010. [3]Schweser et al., Med Phys 2010. [4]de Rochefort et al. MRM 2010. [5]Haacke et al, JMRI 2010. [6]Marques et al., CMRB 2005. [7]Conturo et al., MRM 1990. [8]Hestenes et al., J Res Natl Bureau Standards 1952. [9]Kressler et al., IEEE TMI 2010.

MREIT: from Phase to Conductivity

Eung Je Woo[1], Jin Keun Seo[2], Oh In Kwon[3]
[1]*Kyung Hee University,* [2]*Yonsei University,* [3]*Konkuk University*

Background/Purpose:

Electrical conductivity of a biological tissue conveys diagnostic information, which is not available from other imaging modalities. Magnetic resonance electrical impedance tomography (MREIT) aims to produce cross-sectional images of a conductivity distribution inside an electrically conducting object such as the human body. Current-injection MRI technique is adopted to capture phase images, which include information of induced magnetic flux density. Extracting the induced magnetic flux density data from multiple phase images, one can reconstruct conductivity images. In this presentation, we describe the physical and mathematical principles, novel data collection methods and reconstruction algorithms, experimental techniques and images from phantoms, animals and human subjects.

Methods:

To probe the passive material property of electrical conductivity, we have to either inject current through surface electrodes or induce eddy current by using an external coil. In MREIT, we use electrodes to inject electric current in a form of pulse into an imaging object where the current pulse is synchronized with a chosen pulse sequence. The injected current of a few mA produces a distribution of internal current density **J**, which forms a distribution of internal magnetic flux density **B** in the order nT. Both **J** and **B** are determined by the unknown conductivity distribution of the imaging object and the underlying physical principle can be described by Maxwell's equations. The *z*-component B_z of **B** perturbs the main field of the MRI scanner and causes changes in phase images. Capturing B_z images subject to multiple injection currents after canceling out any systematic phase artifacts, we can reconstruct cross-sectional images of the internal conductivity distribution based on the relationship between the injection current, conductivity and acquired B_z.

Results:

Conductivity images of phantoms including numerous non-biological and also biological objects showed that MREIT can produce absolute conductivity images of 1 mm pixel size with less than 5% error. Postmortem animal experiments revealed two technical problems of tissue anisotropy at low frequency and defective B_z data in a region of MR signal void. From *in vivo* animal and human experiments, we found other difficulties related with chemical shift artifacts and MR system noise. Limiting the amplitude of injection currents to less than 5 mA, we found that imaging of equivalent-isotropic conductivity values inside the human body is feasible.

Conclusion:

From the accumulated knowledge and experiences in MREIT, we can perform *in vivo* conductivity imaging with 1 mm spatial resolution and tens of min temporal resolution using clinical 3 T MRI scanners. We expect that fast imaging of less than 1 mm scan time using less than 1 mA injection current will be possible through technical innovations in pulse sequence design and algorithm development. MREIT is finding clinical applications in early-stage tumor imaging, direct neuro-imaging, mapping of current density and electrical field during electrical stimulations such as DBS, transcranial dc stimulation and electroporation, lesion estimation in RF ablation and so on.

References:

[1] E. J. Woo and J. K. Seo, "Magnetic resonance electrical impedance tomography (MREIT) for high-resolution conductivity imaging," Physiol. Meas., vol. 29, pp. R1-R26, 2008.
[2] J. K. Seo and E. J. Woo, "Magnetic resonance electrical impedance tomography (MREIT)," SIAM Rev., vol. 53, no. 1, pp. 40-68, 2011.
[3] J. K. Seo, D. H. Kim, J. Lee, O. I. Kwon, S. Z. K. Sajib and E. J. Woo, "Electrical tissue property imaging using MRI at dc and Larmor frequency," Inv. Prob., vol. 28, 084002, 2012.
[4] J. K. Seo and E. J. Woo, Nonlinear Inverse Problems in Imaging, Chichester, UK: Wiley, 2013.

Estimating White Matter Anisotropy: Symmetry Considerations and an Analysis of Susceptibility Tensor Reconstructions

Cynthia Wisnieff[1], Pascal Spincemaille[2], Tian Liu[3], and Yi Wang[1]
[1]*Cornell University, Ithaca, New York, United States,* [2]*Weill Cornell Medical College, New York, New York, United States,* [3]*Medimagemetric, New York, New York, United States*

Background/Purpose: Susceptibility tensor imaging (STI) examines the macroscopic magnetic anisotropy of molecularly ordered structures with MRI. STI has been investigated in the white matter, WM, of the brain where magnetic anisotropy has been attributed to the organization of myelin bilayers[1-5]. This organization within WM is critical to maintaining the function of neurons that is lost in diseases such as multiple sclerosis (MS)[6]. Many orientations of the subject are necessary for estimating the magnetic susceptibility anisotropy (MSA) from STI limiting its application in vivo. Applying constraints can reduce the number of unknowns in the susceptibility tensor, to estimate the MSA with fewer orientations[1, 3, 5]. Here, we examine the origins of symmetry in STI in phantom experiments and the potential of CSST reconstructions in vivo to investigate MSA in WM.

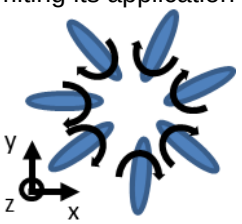

Fig. 1: Arrangement of molecules in WM

Methods: *WM Symmetry* The magnetization of a voxel **M** is the sum of the magnetic moments within the voxel, $\mathbf{M} = 1/\mu_0 \sum_a \boldsymbol{\beta}_a \mathbf{B}_0$, where $\boldsymbol{\beta}_a$ is the magnetic polarizability tensor of a molecule. Let $\boldsymbol{\beta}_a = \mathbf{R}_a \boldsymbol{\beta} \mathbf{R}_a^T$, where $\boldsymbol{\beta} = diag(\beta_1, \beta_2, \beta_3)$ is in the molecular frame(xyz) and $\mathbf{R}_a$ is the rotation to the voxel frame (XYZ). 1) In a tissue made of anisotropic molecules with no particular molecular orientation, Schur's lemma[7] leads to a scalar macroscopic susceptibility: $\chi_{iso} = n\mathbf{I}((\beta_1 + \beta_2 + \beta_3)/3)$ Eq.1, where n is the number of molecules in the voxel and **I** is the identity matrix. 2) In a realistic model of MW, myelin has radial symmetry (Fig. 1): the β_3 component lies in the transverse plane, while the lipid is freely oriented about the fiber axis and β_3 axis: $\mathbf{R}_a = \mathbf{R}_z(\phi_a)\mathbf{R}_x(\theta_a)\mathbf{R}_z(\psi_a)$ where $\mathbf{R}_z$ is free rotation about the z axis and $\mathbf{R}_x$ is a rotation about the x axis with $\theta_a = \pi/2$. This leads to $\chi_{WM} = n\mathrm{diag}((\beta_1 + \beta_2 + 2\beta_3)/4, (\beta_1 + \beta_2 + 2\beta_3)/4, (\beta_1 + \beta_2)/2)$ Eq.2. In STI[3], χ is the inverse solution to $\Delta(\mathbf{k}) = \frac{\hat{\mathbf{b}} \cdot \left(FT(\chi) \cdot \hat{\mathbf{b}}\right)}{3} - \hat{\mathbf{b}} \cdot \mathbf{k} \frac{\mathbf{k} \cdot \left(FT(\chi) \cdot \hat{\mathbf{b}}\right)}{\mathbf{k}^2}$ Eq.3. where Δ is the relative difference field in k-space and $\hat{\mathbf{b}}$ is the B_0 direction relative to subject orientation, which requires 6 parameters to describe the susceptibility tensor. The CSST[5, 8, 9] is an inverse solution to Eq. 3 where $\chi = \mathbf{R}^T \chi_T \mathbf{R}$, Eq. 4 χ_T =diag($\chi_\perp, \chi_\perp, \chi_\parallel$) in the tensor frame and **R** is the rotation from the tensor frame to the subject frame reducing the number of parameters for χ to 2.

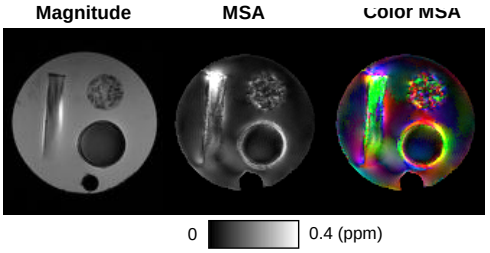

Fig. 2: From left to right, the magnitude image, estimated MSA and principle STI eigenvector weighted by the MSA measured from the carbon fiber phantom.

MRI Phantom 16 orientations were acquired on a phantom containing whole and finely cut carbon fiber (CF) with a multi-echo gradient echo data with a 1mm^3 isotropic resolution (TR/spacing/#Echoes=88ms/3.2ms/10) on a GE 3T scanner for STI. MSA is calculated as $MSA = \lambda_1 - (\lambda_2 + \lambda_3)/2$, when the eigenvalues, λ, are ordered from signed maximum to minimum.

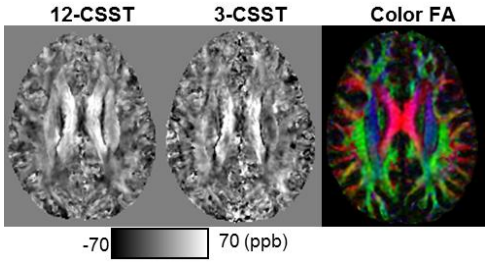

Fig. 3: CSST reconstructions in a volunteer showing the estimated MSA from a reconstruction with 12 and 3 orientations respectively and the registered Color FA of the same slice showing the orientation of the WM fiber tracts[5].

Table 1:Measured MSA across volunteers[5], ppb.

	SCC	BCC	OR
Subject 1	5 ± 21	20 ± 38	30 ± 24
Subject 2	14 ± 12	31 ± 24	30 ± 22
Subject 3	8 ± 16	22 ± 23	31 ± 22
Subject 4	-7 ± 18	37 ± 24	27 ± 23

Results: Estimated MSA: CF Bar: 0.46±0.15ppm, Ring: 0.32±0.04ppm, and Cut: 0.13 ±0.06ppm, showing reduced MSA In the cut CF compared to the ring or bar.

Discussion: The analysis with Schur's lemma indicates that both molecular anisotropy and macroscopic organization order are needed to observe bulk cylindrically symmetric MSA with MRI. As demonstrated in the CF phantom, Fig. 2, a reduction in the macroscopic order of molecular organization leads to reduced MSA observed in STI in the cut versus the whole CF in the ring or bar. The condition number, showing the maximum expected error propagation in the CSST reconstruction, is highly sensitive to relative angles between fiber and acquired orientations[5]. Further, human data show it is possible to consistently reconstruct the CSST with as few as 3 orientations for WM fibers[5], reproduced in Fig.3 and Table 1. These studies demonstrate the sensitivity of STI and CSST to the MSA of molecularly ordered regions such as CF and the WM in the human brain despite of the sensitivity of the reconstructions to the MRI acquisitions. These studies further demonstrate the potential of such techniques to noninvasively detect the MSA in vivo as a possible biomarker of healthy WM.

References: 1.Li, W., et al., NeuroImage, 2012. **59**(3): p. 2088-97.2.Li, W., B. Wu, and C. Liu, Proc. Intl. Soc. Mag. Reson. Med., 2011. **19**: p. 121.3.Liu, C., Magn Reson Med, 2010. **63**(6): p. 1471-7.4.Liu, C., et al., NeuroImage, 2012. **59**(2): p. 1290-8.5.Wisnieff, C., et al., NeuroImage, 2013.6.Keough, M.B. and V.W. Yong, Neurotherapeutics, 2012.7.Hammermesh, M., *Group Theory and Its Application to Physical Problems*. 1962, New York: Dover Publications, Inc.8.Li, X., et al., NeuroImage, 2012. **62**(1): p. 314-30.9.Wharton, S. and R. Bowtell, Proc. Intl. Soc. Mag. Reson. Med., 2011. **19**: p. 4515.

Mapping electric tissue properties using complex B1-mapping

Ulrich Katscher, Philips Research Europe – Hamburg, Roentgenstr. 24, 22335 Hamburg, Germany

Introduction

The electric properties of human tissue, i.e., the electric conductivity σ and permittivity ε, might be used as additional diagnostic parameters or might be helpful for the prediction of the local SAR during MR measurements. "Electric Properties Tomography" (EPT) derives the patient's electric properties using a standard MR system, measuring the spatial transmit (TX) sensitivity distribution of the applied RF coil [1-8]. Thus, EPT does not apply externally mounted electrodes, currents, or RF probes, as in competing techniques. The spatial resolution of the reconstructed σ and ε is of the order of the spatial resolution of the measured MR images. EPT is quantitative MR, i.e., it yields absolute values of σ and ε. Phantom experiments have proven the principle feasibility of EPT, and volunteer brain measurements underline its *in vivo* feasibility [5,6]. Clinical studies are started with preliminary, but encouraging results [9-12].

Theory / Methods

The Helmholtz equation derives σ and ε from the circularly polarized magnetic field $\underline{B_1} = B_1 \exp(i\varphi)$ via

$$\underline{\kappa}(\mathbf{r}) = \frac{-\Delta \underline{B}_1(\mathbf{r})}{\mu_0 \omega^2 \underline{B}_1(\mathbf{r})} \qquad (1)$$

with $\underline{\kappa} \equiv \varepsilon - i\sigma / \omega$ (ω the Larmor frequency). Equation (1) is valid in regions, where the local, spatial variation of $\underline{\kappa}$ is sufficiently small, e.g., inside compartments with constant $\underline{\kappa}$. Equation (1) has to be applied to the $\underline{B_1}$ of the TX RF coil used for the MR measurement. The amplitude $|\underline{B_1}|$ can be measured with standard B_1 mapping sequences. The phase φ can be estimated by cutting in half the transceive phase of a MR image measured with a quadrature volume coil, assuming that the TX phase of this coil resembles its receive (RX) phase with switched polarization (so-called "transceive-phase assumption"). The measured transceive phase has to be free of unwanted phase contributions, unrelated to RF penetration. Particularly, the transceive phase must not contain any contributions from B_0, i.e., any off-resonance effects. The easiest way to exclude off-resonance effects is the use of refocusing pulses, i.e., sequences based on (turbo-)spin echos. The transceive phase of field-echo based sequences includes off-resonance effects, which can be removed by any kind of B_0 mapping. On the other hand, sequences with balanced gradients (steady-state-free-precession, SSFP) are known to have benign off-resonance behavior. As long as B_0 inhomogeneities are too small to cause the well-known banding artefacts, the SSFP transceive phase resembles the transceive phase of spin echo sequences fairly well. Thus, if applicable, SSFP seems to be the sequence of choice for EPT transceive phase measurements [16].

The problem of deriving φ from the transceive phase can be solved analytically by an approach sometimes called "Local Maxwell Tomography" (LMT) [13-15]. LMT is based on the insight that the reconstructed $\underline{\kappa}$ must not depend on the applied RF coil, particularly, the elements of a TX coil array. This condition yields an additional equation enabling the separation of TX and RX phase.

For moderate main field strengths, $|\underline{B_1}| = \text{const}$ can be assumed, and Eq. (1) simplifies to "phase-based" EPT [5,6]

$$\sigma(\mathbf{r}) = \frac{\Delta\varphi(\mathbf{r})}{\mu_0 \omega} \; . \qquad (2)$$

Phase-based EPT reveals two features invaluable for clinical applications: (1) The linearity of Eq. (2) supersedes the derivation of φ from the transceive phase, thus allowing arbitrary combinations of RF TX and RX coils. (2) Skipping the need of mapping $|\underline{B_1}|$, which is typically a rather lengthy scan, can significantly speed up the scan time required for EPT [16].

The impact of B_0 on EPT and the related question of B_0 optimal for EPT is a non-trivial task [17]. Obviously, higher SNR can be expected with increasing B_0. This advantage is counterbalanced by the increasing violation of the assumption $|\underline{B_1}| = \text{const}$ for Eq. (2) or the transceive phase assumption, respectively. According to [17], the optimal tradeoff between SNR and reconstruction accuracy seems to be given at $B_0 = 3\text{T}$ for conductivity imaging. For permittivity imaging, the highest available B_0 seems to be optimal.

Results

Water-based phantoms with different conductivities (adjusted via NaCl concentration) and permittivities (adjusted via 2-propanol concentration) covering the physiologic range served to test the reliability of EPT. The correlations between expected and measured values are above 99% for both, σ and ε ([3,18], see Fig. 1). Furthermore, the brains of healthy volunteers have been investigated [5,6]. Figures 2,3 show σ and ε from two different volunteers. Values of σ and ε averaged over segmented cerebro-spinal fluid, grey and white matter agree with literature values (see, e.g., [19]). The observed inter-subject variability of the mean σ and ε in the mentioned compartments is of the order of 10-20% [5].

Initial EPT results for brain tumors have been reported for 1.5T [9] and 7T [10]. All cases show a tumor conductivity increased roughly by a factor of two compared with the surrounding white matter. A stroke patient was described by [12], showing again a clear increase of the conductivity within the stroke area. Applying EPT to mammography is more challenging than applying EPT to the brain due to typically highly nested gland and fat differing significantly in σ, commonly violating the assumption in Eq. (1) of sufficiently small spatial variation of $\underline{\kappa}$. Locally adapted filter techniques have been suggested to handle these issues ([11], see Fig. 4).

Discussion / Conclusion

Using standard MR systems and standard MR sequences, mapping of the electric properties seems to be clinically feasible, particularly phase-based conductivity imaging. The rapidly evolving field will certainly afford further improved measurement and reconstruction techniques in the near future. The broad spectrum of clinical studies started raise hope that answers will soon be available concerning potential diagnostic benefits of EPT.

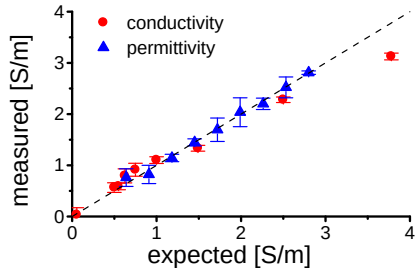

Fig. 1: Phantom results [3,18]. The permittivity is scaled to $\varepsilon\omega \times 10$.

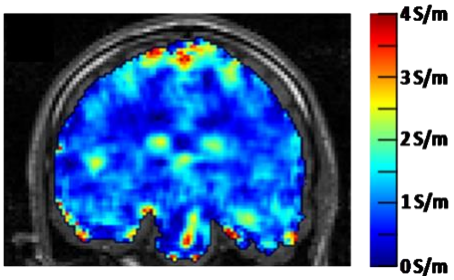

Fig. 2: Reconstructed conductivity of the brain of a healthy volunteer [5].

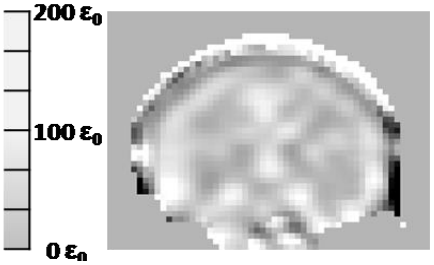

Fig. 3: Reconstructed permittivity of the brain of a healthy volunteer [5].

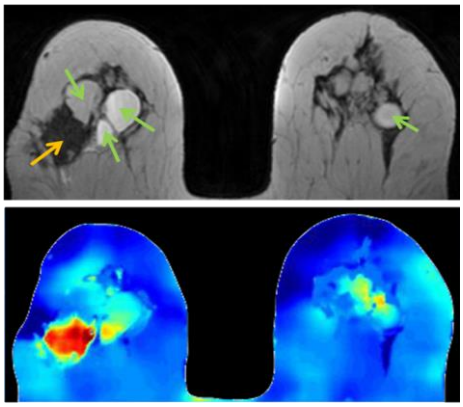
Fig. 4: Breast cancer example [11]. Above: TSE image, showing several cysts (green arrows) and tumor (orange arrow). Below: Reconstructed conductivity of the breast shown above. Low/medium/high conductivity is found for fat/cysts/tumor, respectively.

Acknowledgements

The author cordially thanks Christian Stehning, Tobias Voigt, Christian Findeklee, and Philipp Karkowski for providing significant contributions.

References

[1] Haacke EM Petropoulos LS Nilges EW Wu DH. Extraction of conductivity and permittivity using MRI. Phys Med Biol 1991;36:723-734.

[2] Wen H. Noninvasive quantitative mapping of conductivity and dielectric distributions using RF wave propagation effects in high-field MRI. In Proceedings of SPIE 2003;5030:471-477.

[3] Katscher U, Voigt T, Findeklee C, Vernickel P, Nehrke K, Doessel O. Determination of Electric Conductivity and Local SAR via B1 Mapping. IEEE Trans Med Imaging. 2009;28:1365-1374.

[4] Zhang X, Zhu S, He B. Imaging electric properties of biological tissues by RF field mapping in MRI. IEEE Trans Med Imaging. 2010;29:474-481.

[5] Voigt T, Katscher U, Doessel O. Quantitative Conductivity and Permittivity Imaging of the Human Brain using Electric Properties Tomography. Magn Reson Med. 2011;66:456-466.

[6] van Lier AL, Brunner DO, Pruessmann KP, Klomp DW, Luijten PR, Lagendijk JJ, van den Berg CA. B 1+ Phase mapping at 7 T and its application for in vivo electrical conductivity mapping. Magn Reson Med. 2012;67:552-561.

[7] Bulumulla SB, Lee SK, Yeo DTB. Conductivity and Permittivity Imaging at 3.0 T. Concepts in Magnetic Resonance Part B (Magnetic Resonance Engineering) 2012;41B:13-21.

[8] Seo JK, Kim MO, Lee JS, Choi N, Woo EJ, Kim HJ, Kwon OI, Kim DH. Error Analysis of Nonconstant Admittivity for MR-Based Electric Property Imaging. IEEE Trans Med Imag 2012;31:430

[9] Voigt T, Väterlein O, Stehning C, Katscher U, Fiehler J. In vivo Glioma Characterization using MR Conductivity Imaging. ISMRM 2012;19:127.

[10] van Lier AL, Hoogduin JM, Polders DL, Boer VO, Hendrikse J, Robe PA, Woerdeman PA, Lagendijk JJW, Luijten PR, van den Berg CAT. Electrical Conductivity Imaging of Brain Tumours. ISMRM 2011;19:4464.

[11] Katscher U, Djamshidi K, Voigt T, Ivancevic M, Abe H, Newstead G, Keupp J. Estimation of breast tumor conductivity using parabolic phase fitting. ISMRM 2012;20:3482.

[12] van Lier AL, Kolk A, Brundel M, Hendriske J, Luijten P, Lagendijk J, van den Berg CAT, Electrical conductivity in Ischemic stroke at 7.0 Tesla: A case study. ISMRM 2012;20:3484.

[13] Katscher U, Findeklee C, Voigt T. Single element SAR measurements in a multi-transmit system. ISMRM 2011;19:494.

[14] Sodickson DK, Alon L, Deniz CM, Brown R, Zhang B, Wiggins GC, Cho GY, Eliezer NB, Novikov DS, Lattanzi R, Duan Q, Sodickson LA, Zhu Y. Local Maxwell Tomography Using Transmit-Receive Coil Arrays for Contact-Free Mapping of Tissue Electrical Properties and Determination of Absolute RF Phase. ISMRM 2012;20:387.

[15] Katscher U, Findeklee C, Voigt T. B1-based SAR determination for non-quadrature RF excitation. MRM 2012;68:1911-1918.

[16] Stehning C, Voigt T, Katscher U. Real-Time Conductivity Mapping using Balanced SSFP and Phase-Based Reconstruction. ISMRM 2011;19:128.

[17] van Lier AL, Voigt T, Katscher U, van den Berg CAT. Comparing Electric Properties Tomography at 1.5, 3 and 7 T. ISMRM 2011;19:125 / MRM, in press.

[18] Katscher U, Karkowski P, Findeklee C, Voigt T. Permittivity determination via phantom and in vivo B1 mapping. ISMRM 2010;18:239.

[19] Gabriel S, Lau RW, Gabriel C. The dielectric properties of biological tissues: II. Measurements in the frequency range 10 Hz to 20 GHz. Phys Med Biol. 1996;41:2251-2269.

From relative coil sensitivities to electrical property mapping

José P. Marques[1], Daniel K. Sodickson[2], Christopher M. Collins[2], and Rolf Gruetter[3,4]

1CIBM, University of Lausanne, Lausanne, Vaud, Switzerland, 2Bernard and Irene Schwartz Center for Biomedical Imaging, Department of Radiology, New York University School of Medicine, New York, NY, United States, 3LIFMET - Laboratory for Functional and Metabolic Imaging, EPFL, Lausanne, Vaud, Switzerland,4Department of Radiology, Universities of Geneva and Lausanne, Lausanne, VD, Switzerland

Background/Purpose: All methods to map electrical conductivity (σ) and permittivity (ε) of a sample/tissue using MRI presented to date rely on multiple acquisitions. Particularly, in the case where this calculation relies on the interaction between oscilating magnetic fields and the tissue, these multiple measurements are necessary to compute quantitative magnitude RF transmit fields, B_1^+, and either: (a) make assumptions regarding the phase of the RF field that are not valid at high field strength [1,2,3]; (b) use multiple transmit coils to estimate the absolute RF phase [4]; or compute absolute RF phase by combining B_1^+ maps with receive B_1^- maps [5]. In this work we propose a formalism to compute electrical property maps based solely on relative receive coil sensitivities that can be obtained from any 3D imaging technique and demonstrate the feasibility of this approach in simulations and phantom data.

Theory The Helmholtz equation is valid for both transmit and receive magnetic fields in regions of constant σ and ε. Although absolute B_1^- fields cannot be measured, relative receive field between two coils, $B'^-_{1,i,ref}$, can be measured from any MR acquisition as:

$$B'^-_{1,i,ref}=\frac{Signal_i}{Signal_{ref}}=\frac{B^-_{1,i}}{B^-_{1,ref}}$$

where $Signal_i$ is the signal measured by coil *i*.

Given that the conductivity and permittivity experienced by any of the receive coils is the same, $\left(\frac{\nabla^2 B^-_{1,i}}{B^-_{1,i}}=\frac{\nabla^2 B^-_{1,ref}}{B^-_{1,ref}}\right)$, it is possible to build a set of linear equations $-2\nabla B'^-_{1,i,ref}\cdot\frac{\nabla B^-_{1,ref}}{B^-_{1,ref}}=\nabla^2 B'^-_{1,i,ref}$ which can be solved for the gradients of the unknown absolute reference field, $\nabla B^-_{1,ref}/B^-_{1,ref}$, if four or more receive coils are available. Electrical properties can subsequently be computed by rewriting the Helmholtz equation as a function of $\nabla B^-_{1,ref}/B^-_{1,ref}$:

$$\frac{\nabla^2 B^-_{1,ref}}{B^-_{1,ref}}=\frac{\nabla B^-_{1,ref}}{B^-_{1,ref}}\cdot\frac{\nabla B^-_{1,ref}}{B^-_{1,ref}}+\nabla\cdot\left(\frac{\nabla B^-_{1,ref}}{B^-_{1,ref}}\right)=-\left(\mu\varepsilon\omega^2-i\mu\sigma\omega\right)$$

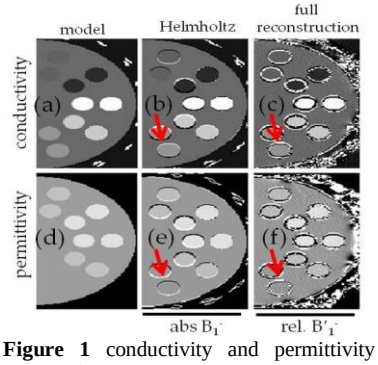

Figure 1 conductivity and permittivity maps of a transverse slice across the numerical phantom are shown in the top and bottom rows respectively. The columns show: (a,d) - modeled maps, (b,e) - maps reconstructed when using the Helmholtz equation assuming B_1^- is fully known; (c,f) reconstructed maps starting from relative receive coil sensitivities using the proposed method. Red arrows highlight the artifacts present in tissue interfaces where the σ or ε are not constant.

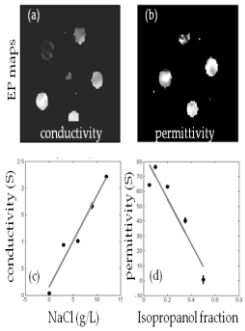

Figure 2 (a) conductivity and (b) permittivity maps of a transverse slice across the compartmentalized phantom are shown. Plot of (c) the conductivity as a function of NaCl concentration and of the permittivity (d) as a function of the isopropanol volume fraction. Error bars represent standard error of the mean within the ROI

Methods: Numerical Simulations - a transceive array with 16 loop elements surrounding a spherical (d=160mm) phantom (σ=0.75 and ε=65) including smaller spheres with varying conductivity (0.2-2.1) and permittivity (40-90) was simulated at 300MHz using XFDTD v6.4 (Remcom, Inc.).

Phantom data was acquired on a 7T MR scanner (Siemens Medical Solutions, Erlangen, Germany) using a 32-element receive array (Nova Medical Inc). 3DGRE sequence parameters: TR/TE= 8/3.6ms; α=10°, res=1x1x1 mm (5 mins); Compartmentalized spherical phantom (d=120mm) water phantom: filled with 0.037g/L $MnCl_2$ and 10% isopropanol and 9 spherical compartments (d=40mm): 5 with 0, 3, 6, 9 and 12 g/L of NaCl,;4 with 5, 20,35 and 50% volume of isopropanol;

Results: Figure 1 shows the results of the numerical simulations, where a high correlation (0.99) was found between the calculated and modeled properties when the boundaries (where Eq.1 is not valid) are neglected. Figure 2a and 2b show masked **σ** and **ε** maps. From the plot of the conductivity (Fig. 2c) as a function of NaCl concentration it was possible to calculate: $\boldsymbol{\sigma_{water}}$**=0.15 S/m** and $\boldsymbol{\sigma_{NaCl}}$ **=0.17 S/m per 1 g/L** which is in agreement with literature [3]. From the plot of the permittivity of water as a function of isopropanol fraction (Fig. 2c) it was possible to calculate $\boldsymbol{\varepsilon_{water}}$**= 85**.

Conclusion: Electrical property mapping based on relative receive sensitivity maps has been demonstrated in simulations and experimentally on phantom data. The main advantages of the methodology are: (a) it is based on a single measurement (which is faster and less prone to subject motion than multiple-measurement approaches); (b) it does not rely on the measurement of B_1^+ maps (whose accuracy and precision is limited)[1-5], or on specific coil/subject setups [1-4]; (c) it is insensitive to practical complications such as frequency inhomogeneities or eddy currents [3]; (d) it can be calculated from the same data as the quantitative magnetic susceptibility maps!

References: [1] Katscher et al. IEEE, **28**, 2009; [2] Voigt et al, MRM, **66**, 2011; [3] van Lier et al, MRM, 67, 2012; [4] Katscher et al, MRM, 2012; [5] Sodickson et al, ISMRM, 2012,387

What is the Relationship Between MR Signal Phase and Underlying Tissue Magnetic Susceptibility?

Dmitriy A. Yablonskiy

Washington University, St. Louis, MO, USA

During the last several years there has been increased interest to the issues related to biological tissue magnetic susceptibility, especially in the brain. The focus of many publications is on developing MRI-based techniques to quantify tissue magnetic susceptibility from measuring the Gradient Echo (GE) signal phase. To successfully accomplish this task, we first need to understand the relationship between the GE signal phase and underlying tissue magnetic susceptibility or, more precisely, tissue magnetic architecture - the structural (geometric) arrangement of the main tissue components (proteins, lipids, iron, etc.) that, as far as MRI is concerned, act as magnetic susceptibility inclusions.

An effect of external magnetic field $\mathbf{B_0}$ on tissue is usually described in terms of local tissue magnetization $\mathbf{m}(\mathbf{r})$ that in diamagnetic and paramagnetic substances is proportional to $\mathbf{B_0}$ with coefficient of proportionality called magnetic susceptibility $\chi(\vec{r})$ (note that in white matter the magnetic susceptibility can be anisotropic (1, 2)). This induced magnetization produces its own magnetic field $\mathbf{h}(\mathbf{r})$. If the magnetization $\mathbf{m}(\mathbf{r})$ is known, one can use Maxwell equations to calculate $\mathbf{h}(\mathbf{r})$. An MR signal is generated by water molecules diffusing in this inhomogeneous magnetic field and accumulating phases $\varphi_n[\mathbf{r}(t)] = \gamma\int_0^t h_z[\mathbf{r}_n(t')]dt'$, where h_z is a projection of induced magnetic field on $\mathbf{B_0}$ and $\mathbf{r}_n(t')$ describes a trajectory of *n*-th diffusing water molecule. Then, the total MR signal can be calculated as a sum over all water molecules: $S(t) = S(0)\cdot\sum_n \exp(-i\varphi_n[\mathbf{r}(t)])$. Calculating this signal for real biological structures is an extremely complicated problem and can only be accomplished by using certain assumptions and simplifications that will be discussed in my presentation.

1. <u>*Lorentzian sphere approach.*</u> In this approach, the real magnetic field $\mathbf{h}(\mathbf{r})$ created by the tissue is substituted by a field that would exist if diffusing water molecules were moving inside a *hollow sphere* carved out in the tissue (3, 4). While this the most commonly used approximation is justified for liquid solutions in the presence of randomly distributed magnetic susceptibility inclusions, e.g. contrast agent, it cannot be used in the presence of prolonged cells, e.g. axons.
2. <u>*Generalized Lorentzian Approach* GLA)</u> (5). If the magnetic environment is not random (as in the brain which is highly organized cellular structure), the calculation of the effect of magnetic field $\mathbf{h}(\mathbf{r})$ should take into account the symmetry of this environment. Specifically, the contribution to the real magnetic field $\mathbf{h}(\mathbf{r})$ from longitudinally-arranged structures, such as neurofilaments and myelin layers in axons, can be calculated by substituting $\mathbf{h}(\mathbf{r})$ by a field that would exist if diffusing water molecules were moving inside a *hollow cylinder* carved out in the tissue (5, 6). The contribution to $\mathbf{h}(\mathbf{r})$ from randomly distributed structures can still be accounted for by using Lorentzian sphere. The GLA explains the "WM darkness effect" (5, 6) — the lack of phase contrast between WM and CSF (reported in (5, 7)), despite substantial differences in their molecular content and *total* magnetic susceptibilities. The important consequence of GLA is also a prediction of the anisotropy of phase contrast in WM – a correlation between the MR signal phase and orientation of neuronal fibers with respect to $\mathbf{B}_0$ (5). Importantly, this effect is due to the anisotropic structure of cells, e.g. axons, and exists even in the case when the magnetic susceptibility of these structures is isotropic.
3. <u>*Modeling approach.*</u> The previous approaches assume that the MR signal from a tissue can be described in terms of a single compartment/component model. A more detail description should take into account the presence of different compartments (such as intra- and extra-cellular water) as well as anisotropy of magnetic susceptibility of lipid membranes (8). For axons, such models have recently been developed in Refs. (9, 10).

Conclusion: Proper consideration of brain tissue structure at the cellular level and its influence on MR signal phase is essential for QSM.

References:

1. Lee J, et al. Sensitivity of MRI resonance frequency to the orientation of brain tissue microstructure. PNAS, 2010;107(11):5130-5.
2. Liu CL. Susceptibility Tensor Imaging. Magnetic Resonance in Medicine. 2010;63(6):1471-7.
3. Chu SC, Xu Y, Balschi JA, Springer CS, Jr. Bulk magnetic susceptibility shifts in NMR studies of compartmentalized samples: use of paramagnetic reagents. Magn Reson Med. 1990;13(2):239-62.
4. Durrant CJ, Hertzberg MP, Kuchel PW. Magnetic susceptibility: Further insights into macroscopic and microscopic fields and the sphere of Lorentz. Concepts in Magnetic Resonance Part A. 2003;18A(1):72-95.
5. He X, Yablonskiy DA. Biophysical mechanisms of phase contrast in gradient echo MRI. PNAS, 2009;106(32):13558-63.
6. Yablonskiy DA, Luo J, Sukstanskii AL, Iyer A, Cross AH. Biophysical mechanisms of MRI signal frequency contrast in multiple sclerosis. PNAS, 2012;109(35):14212-7.
7. Duyn JH, van Gelderen P, Li TQ, de Zwart JA, Koretsky AP, Fukunaga M. High-field MRI of brain cortical substructure based on signal phase. PNAS, 2007;104(28):11796-801.
8. Lounila J, Ala-Korpela M, Jokisaari J, Savolainen MJ, Kesaniemi YA. Effects of orientational order and particle size on the NMR line positions of lipoproteins. Phys Rev Lett. 1994;72(25):4049-52.
9. Wharton S, Bowtell R. Fiber orientation-dependent white matter contrast in gradient echo MRI. PNAS, 2012;109(45):18559-64. Epub 2012/10/24.
10. Sukstanskii AL, Yablonskiy DA. On the role of neuronal magnetic susceptibility and structure symmetry on gradient echo MR signal formation. Magnetic Resonance in Medicine. 2013:DOI 10.1002/mrm.24629.

Regularization Parameter Estimation for Biomedical Imaging

Rosemary Renaut[1], Yi Wang[2],

[1]Arizona State University, [2] Cornell University,

Background/Purpose:

Reconstruction of images from biomedical data may be formulated as the solution to a linear system of equations $Ax \approx b$ in which the matrix A describes the underlying process for the image acquisition; x is the desired image and b the set of measured data with noise. Ill-posedness manifests in ill-conditioning of matrix A, and is characterized by solutions which are unstable to noise in the data, and are not uniquely defined. In finding a feasible solution it is essential to augment the fidelity with a regularization term, R(x), describing the prior information, thus yielding the solution $x=\text{argmin}\ \{||\ Ax-b||^2_W + \lambda^2 R(x)\}$. Here weighting matrix W is introduced to account for inverse covariance properties of the noise in the measurements b, when available; and $\lambda>0$ is a regularization parameter. In contrast to a formulation in which λ is regarded as a Lagrangian multiplier, carrying no information about noise distributions on the solution and prior information, in general the choice for λ is not uniquely defined. Indeed, it can be appropriate to include λ within the definition of R(x) so that the scalar λ is regarded as an unknown multi-parameter vector, which weights different components in the regularization. Many approaches to find the *optimal* regularization parameter(s) are available typically by accounting for both the properties of the noise in the data and the quality of prior information quality (*1, 2*); thus avoiding exhaustive parameter search. This talk reviews methods of choosing regularization parameters to identify a statistically valid and computationally feasible method for a given application.

Methods:

For this overview we focus on regularizations of the form $R(x)= ||x-x_0||_p$ where x_0 is prior information on x, p=2 leads to the traditional Tikhonov regularization; while sparsity, p=0, is obtained by approximating with the choice p=1. Alternative forms introduce a mapping on x, Dx, which amounts to expressing the solution in a different basis such as the derivative of x or a specific wavelet basis. Often adopted approaches for finding the regularization parameter(s) include the discrepancy principle, which finds solution x so that the measure of the fidelity roughly approximates the noise in the measurements, the L-curve method that trades off the fidelity $||\ Ax-b||^2$ and regularizer R(x) often revealed as a L shape on a log-log plot, and the principle of generalized cross-validation. Less used, but robust and efficient is the χ^2 technique (1). In this overview we assess these standard techniques as well as the less used method of (1) when used with p=1,2 regularizers.

Results:

Our results contrast the modeling approach for finding the regularization parameter (1), as compared to exhaustive search, or less sophisticated techniques such as the L-curve. We will show that the correct inclusion of statistical information, as provided through the χ^2 technique, leads to an efficient and effective algorithm for finding the regularization parameter; for both p=1 and p=2 regularizers.

Conclusion:

The correct inclusion of statistical and prior information in image reconstruction algorithms can improve computational feasibility for finding biomedical images.

References:

1. R. A. Renaut, I. Hnetynkova, J. Mead, Regularization parameter estimation for large-scale Tikhonov regularization using a priori information. *Computational Statistics & Data Analysis* **54**, 3430 (2010).
2. F. Bauer, M. A. Lukas, Comparingparameter choice methods for regularization of ill-posed problems. *Mathematics and Computers in Simulation* **81**, 1795 (2011).

Pulse Sequence Consideration

Wei Li[1], Bing Wu[1,3], Chunlei Liu[1,2]
[1]*Brain Imaging & Analysis Center,* [2]*Radiology, Duke University, Durham, NC, USA,* [3]*GE Healthcare, Beijing, China*

Background/Purpose: Gradient-echo (GRE) signal phase and its derived quantitative magnetic susceptibility provide invaluable information of brain anatomical details, chemical composition, especially myelin and iron, and tissue microstructure (review [1]). They have found many promising applications in the study of neurological diseases, e.g. cerebral micro-bleeds, Parkinson's diseases, multiple sclerosis and so on (review [2]). However, traditional pulse sequences for phase and susceptibility mapping usually suffer from long scan time due to the requirement of 3D volume acquisition and long echo time for the accumulation of phase contrast. A variety of novel sequences, using e.g. spiral [3] and EPI trajectories [4], as well as traditional Cartesian trajectory with parallel imaging acceleration, has been proposed and applied to speed up the scan. The scan parameters of each sequence were also often adjusted to meet the particular needs of different applications. Here, we will make effort to address two practical but important questions regarding the choice of pulse sequences and scan parameters for phase and susceptibility mapping: (1) what are their differences in terms of signal-to-noise ratio (SNR), scan time, reliability and accuracy? and (2) whether and how phase and susceptibility contrasts are affected by the scan parameters, including flip angle, TR and TE?

Methods: We have developed three different sequences for fast phase and susceptibility imaging, including multi-echo spiral (ME-Spiral), multi-echo EPI (ME-EPI) sequences, and multi-echo SPGR sequence using traditional Cartesian sampling with GRAPPA acceleration (GRAPPA-ME-SPGR). We compared their accuracy in susceptibility quantification by comparing to the conventional SPGR sequence, the gold standard. We also evaluated their SNR, and reliability by examining the image quality of a series of scans. We further assessed the dependence of phase contrast on image acquisition parameters using a conventional multi-echo SPGR (ME-SPGR) sequence, with varying TR and flip angles. Two datasets were acquired. The first dataset has multiple flip angles with flip angle = 5º, 20º, 40º and 60º, and the second dataset has multiple TRs with TR = 46 ms, 150 ms and 1s. The echo times were from 4 ms to 36 ms.

Results: Both ME-Spiral and ME-EPI sequences are more effective in accelerating the image acquisition than the conventional GRAPPA-ME-SPGR sequence. The spiral sequence allows for fast image acquisition with 1 mm isotropic resolution and a 192x192x120 mm^3 volume within 2.5 min, with similar SNR comparing to that of SPGR sequence. However, the ME-Spiral sequence sometimes suffers from susceptibility-induced blurring artifacts. Comparing to the ME-spiral sequence, the ME-EPI sequence provides higher reproducibility, however with slightly lower SNR. As such, we have to increase the voxel size to improve the SNR. The MR-EPI sequence can provide phase and susceptibility maps with a matrix size of 256x256x64 and a voxel size of 0.86x0.86x2 mm^3 within 3 min. The susceptibility values of major brain structures determined by both the spiral sequence and the EPI sequence are linearly correlated with those determined by the standard SPGR sequence. The GRAPPA-ME-SPGR sequence provides the highest reproducibility with longer scan time comparing to the spiral and EPI sequences. A typical scan with a matrix size of 288x254x54 and spatial resolution of 0.76x0.76x2 mm^3 will require 6 min of scan time. In addition, the GRAPPA-ME-SPGR and ME-SPGR sequences are particularly good for high resolution brain imaging. While it is known that GRE signal phase evolves in a nonlinear phase fashion [5], we found that phase contrast between cortical gray and white matter also has a profound dependence on TR and flip angle using the aforementioned scan parameters. This is due to the fact that different intra- and intercellular compartments have different frequency shifts.

Conclusion: Each of the studied susceptibility imaging sequences, including ME-Spiral, ME-EPI and GRAPPA-ME-SPGR, has its own advantages and disadvantages in terms of scan time, SNR, and reproducibility. Although the three different sequences give approximately the same susceptibility values with the current selection of scan parameters, our results did reveal a profound dependence of phase and susceptibility contrasts on scan parameters, including TE, TR and flip angle. While these pulse sequences provides a spectrum of choices for various research and clinical applications, maintaining consistent selection of pulse sequence and scan parameters are critical to ensure inter-subject and inter-study reproducibility.

References: [1] Duyn, J Magn Reson 2013, 229: 198-207. [2] Reichenbach, Neuroimage, 2012, 62:1311-1315. [3] Wu et al, NeuroImage 2012, 59: 297-305. [4] Wu et al, Proc ISMRM 2013: 4236. [5] Schweser, Proc ISMRM 2011. 4527

Understanding the anisotropic properties of the myelin sheath using a hollow cylinder fiber model

Samuel Wharton[1], Richard Bowtell[1]
[1]*Sir Peter Mansfield Magnetic Resonance Centre, School of Physics and Astronomy, University of Nottingham, UK*

Background/Purpose: Recent studies have shown that there is a direct link between the orientation of the nerve fibers in white matter (WM) with respect to the magnetic field and the contrast observed in magnitude and phase images [1-2]. It has recently been suggested that the myelin sheaths that surround axons are the dominant source of WM contrast in GE MRI [3-4]. Creating an accurate model for characterizing the effect of the myelin sheath on the evolution of the magnitude and phase of the NMR signal is consequently an essential step toward fully understanding WM contrast and its relationship to fiber orientation. In this talk, I will be discussing the results and implications of recent work by our group showing that the fiber orientation dependence of the magnitude and phase of signals acquired from WM in vivo can be accurately characterized by modeling the myelin sheath as a hollow cylinder composed of material having an anisotropic susceptibility that is described by a tensor with a radially oriented principal axis. This hollow cylinder fiber model (HCFM) is a two-pool model in which the water in the sheath (cylinder annulus) has a reduced T_2 relaxation constant and effective spin density relative to its surroundings [5]. As part of this work, a new technique called frequency difference mapping (FDM) was utilized to generate local phase based contrast relating to the underlying fiber orientation.

Methods: Analytical expressions for the field perturbation due to the HCFM were formed. Fig. 1 shows maps of the frequency perturbations produced by the hollow cylinder, with its principal axis parallel (θ = 0°) and perpendicular (θ = 90°) to B_0, as a result of three different mechanisms: isotropic susceptibility (χ_I), exchange (E), and radial anisotropic susceptibility (χ_A). Interestingly, the anisotropic offset induces a large homogeneous field offset inside the axonal compartment of the HCFM at θ = 90°. These field maps then formed the basis of signal evolution simulations that were compared to magnitude and FDM data acquired in vivo at 7T. Fig 2 shows representative high resolution FDM data (C) that was formed by subtracting a long TE frequency map (B) from a short TE frequency map (A). The corresponding DTI-based fiber orientation map (acquired at 3T) is shown in Fig. 2D.

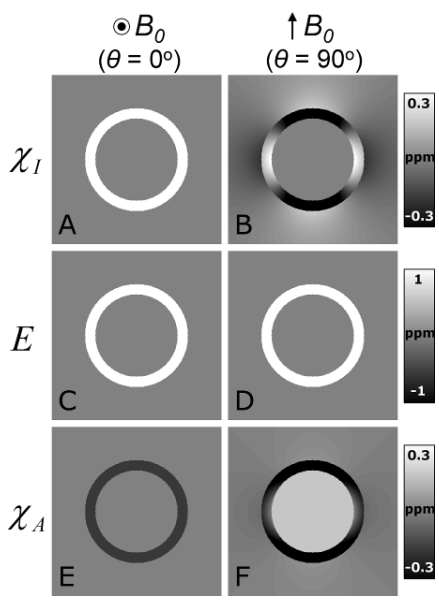

Fig. 1 HCFM field map simulations for χ_I = χ_A = E = 1ppm.

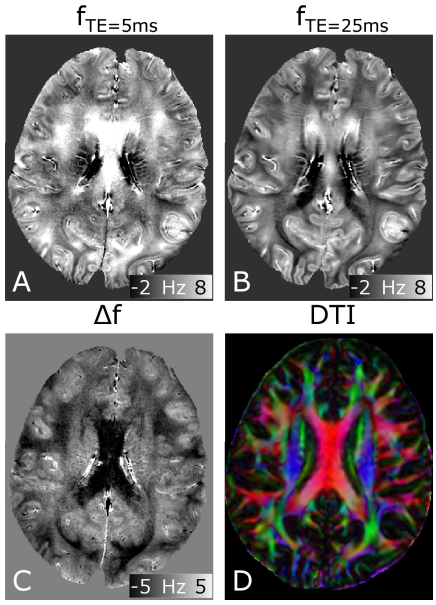

Fig. 2 FDM data acquired at 7T

Results: Through comparisons between simulated and in vivo data, the HCFM was shown to accurately characterize fiber orientation dependent signal evolution in WM. Fitted parameter values for the HCFM included a short T_2 associated with myelin water (~8 ms) and a large diamagnetic radially oriented anisotropic susceptibility (χ_A ~ -0.12 ppm) [5]. Interestingly, this anisotropy generates an average frequency offset that is positive in the myelin, but negative inside the lumen. Reduction of the signal from the myelin compartment consequently leaves a negative local frequency offset in WM relative to GM, which is strongest in fibers that are perpendicular to the field. Frequency difference mapping forms a powerful method for investigating WM microstructure; unlike phase mapping, it is insensitive to nonlocal frequency offsets produced by large anatomical structures and by external sources of field inhomogeneity, and in contrast to susceptibility mapping and susceptibility tensor imaging, it does not require the solution of an ill-posed inverse problem.

Conclusions: The HCFM offers new insight into the complicated fiber orientation-dependent signal behavior observed in WM due to the highly anisotropic properties of the myelin sheath. Also, FDM has the potential to be a useful tool for investigating microstructure in vivo.

References: [1] van Gelderen et al. 2011. 67, 110-117. [2] Lee et al. PNAS. 2010. 107, 5130-5135 [3] Lee et al. 2011. Neuroimage. 59, 3967-3975. [4] Liu et al. Neuroimage. 2011. 56, 930-938 [5] Wharton and Bowtell. PNAS. 2012. 109, 18559-18564.

Magnetic Susceptibility Atlas Development

Issel Anne L. Lim, Andreia V. Faria, Xu Li, Johnny T. Hsu, Raag D. Airan, Susumu Mori, ***Peter C.M. van Zijl***
Johns Hopkins University School of Medicine, Neurosection, Division of MRI Research, Dept. of Radiology, Baltimore, MD, 21205
F.M. Kirby Research Center for Functional Brain Imaging, Hugo Moser Research Institute at Kennedy Krieger, Baltimore, MD, 21205

Purpose: Brain iron concentration has been reported to change in several neurodegenerative disorders Quantitative Susceptibility Mapping (QSM) methods have shown correlations between magnetic susceptibility and iron content in brain gray matter (GM).[1-4] The average susceptibility for a brain structure currently is determined through manual delineation. For large data sets (group studies) analysis would take a long time and be limited by human error. An alternative approach uses stereotaxic atlases as a frame of reference; automated coregistration between subject and atlas allows for efficient segmentation of the subject brain. For example, the Eve atlas from Johns Hopkins University is a single-subject human brain with 1mm3 isotropic resolution in standard Montreal Neurological Institute (MNI) coordinates.[5] Regions of interest (ROIs) in the DTI-based White Matter Parcellation Map (WMPM) in this atlas are based on white matter orientation and tract structures. However, when overlaid on QSM images, these ROIs do not align perfectly with GM structures, which have very low fractional anisotropy. After defining GM regions on QSM maps to create a new deep GM parcellation map (DGMPM) and combining these ROIs with the WMPM, we created the "EvePM," or "Everything" Parcellation Map, allowing automated segmentation of QSM images for over sixty brain regions in less than 24 hours for 5 subjects. The average susceptibility for GM regions can then be correlated with brain iron concentration if a calibration curve is available, for which literature values from age-dependent postmortem studies were used.[6]

Methods: Five healthy male subjects (age 30-33) were studied after IRB approval and written informed consent on a 3T Philips system (dual-channel body-coil excitation, 32-channel head receive). Subjects were scanned at four orientations with respect to the B_0 field.[1,3,7] Phase images were acquired with a 3D ten-echo GRE sequence (SENSE = 2x1x2, TR = 70ms, TE1 = 6ms, ΔTE = 6ms, α = 20°, fat suppressed, 9:19min). An MPRAGE was also acquired (3D GRE turbo-field echo readout factor = 184, shot interval = 3500ms, SENSE = 1x1x2, TI/TE/TR = 1000/3.2/7.0ms, α=8o). MPRAGE and GRE covered the entire brain (acquired resolution = 1.2mm isotropic). Using MATLAB, susceptibility maps were calculated using COSMOS[1,7] with Laplacian-based phase unwrapping.[2] The average susceptibility was referenced using a grouped deep WM structure ROI set to -0.03ppm, corresponding to average of 0ppm in CSF. As a consequence, brighter contrast in the QSM indicates structures more paramagnetic than CSF7. Accuracy of the segmentation methods was assessed using a kappa analysis, with one human rater designated as the gold standard. Brain iron concentrations determined as a function of age in the globus pallidus (GP), putamen (PT), and caudate nucleus (CN) from Hallgren and Sourander6 were used to linearly calibrate susceptibility versus iron, from which the brain iron concentration for other deep GM regions could be determined (Fig. 2b).

Results: Figure 1 shows the axial, sagittal, and coronal planes of the parcellation maps. The kappa statistic was 0.85 between automated and manual segmentation, and 0.89 between human raters, suggesting "almost perfect" agreement between all methods. Figure 2a shows the magnetic susceptibility for nine deep GM structures in our five 30- to 33-year-old volunteers, which was linearly correlated for the GP, PT, and CN with age-based iron concentration from[6] (Fig. 2b, R2 = 0.997). The average susceptibility for other GM ROIs was plotted along this line (Fig. 2b), providing an estimate of their average brain iron concentration (Fig. 2c).

Discussion: The increase in contrast and spatial resolution provided by QSM versus DTI improved the definition of deep GM ROIs in the Eve atlas, allowing

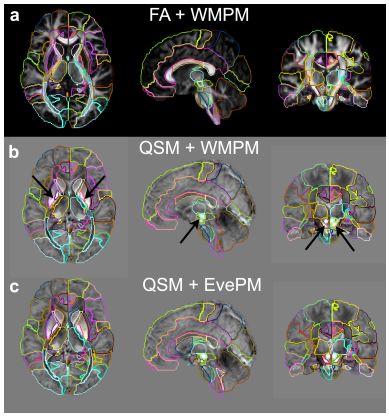

Figure 1: (a) WMPM on FA map in Eve Atlas. (b) Misaligned ROIs from WMPM on QSM. (c) Resolved ROIs in EvePM.

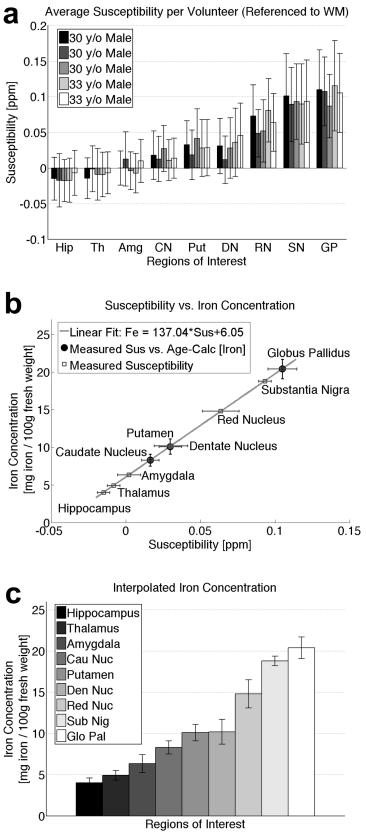

Figure 2: (a) Average susceptibility in GM. (b) Linear correlation: susceptibility and [iron]. (c) Estimated [iron].

automated reproducible quantification of magnetic susceptibility. We found our automated segmentation to have comparable accuracy to manual multiple-rater delineation and to be more efficient; manual delineation of twelve ROIs across five subjects took three weeks, whereas automated delineation of >60 ROIs took less than 24 hours. Brain iron concentration is not straightforward to determine, as it changes with age. Future work involves measuring baseline susceptibility at different ages to determine brain iron concentration throughout development and aging.

Conclusion: This atlas provides a time-efficient tool for automatedly co-registering and segmenting many regions of interest for quantitative susceptibility data, thereby allowing the correlation of susceptibility measurements with brain iron concentration, which has been suggested to be a potential noninvasive biomarker of neurodegeneration or aging. Images exhibiting different types of contrast that have been coregistered to the atlas can also be automatedly segmented, allowing for direct comparison of quantitative metrics between different modalities.

References: 1) Liu T, et al. MRM 2009;61:196-204. 2) Li W, et al. NeuroImage 2011;55:1645-56. 3) Wharton S & Bowtell R. NeuroImage 2010;53:515-25. 4) Schweser F, et al. NeuroImage 2011;54:2789-807. 5) Mori S, et al. Brain 2008;40:570-82. 6) Hallgren B & Sourander P. J. Neurochem 1958;3:41-51. 7) Li X, et al. NeuroImage 2012;62:314-30.
Funding: NIH-P41 EB051909, NIH 5 T32 MH015330.

Supported by NIH grant P41EB015909 and 5 T32 MH015330

Regularization with Total Generalized Variation

Kristian Bredies[1], Florian Knoll[2]
[1]*University of Graz,* [2]*New York University School of Medicine*

Background/Purpose: The solution of inverse problems is often ill-posed, i.e. the reconstructed solution is non-unique or does not stably depend on the data. In this case, regularization is necessary, usually in the form of minimizing a Tikhonov functional. Here, the choice of the regularization functional plays an important role for the qualitative properties of the reconstructions. For imaging data, the *Total Variation* (TV) has become a standard regularizer [1], especially since compressed sensing became popular. The Total Variation, however, is best-suited for modeling piecewise constant images. This assumption is often violated, for instance for images of biological tissue, resulting in unwanted blocking and staircasing artifacts in the reconstructions. The concept of the *Total Generalized Variation* (TGV) resolves this issue: It is capable of efficiently representing piecewise smooth images [2]. When used as a regularizer, it leads to reconstructions with a high visual quality where in particular, edges are preserved and staircasing artifacts are absent [3].

Methods: The Total Generalized Variation of second order can itself be seen as the solution of an appropriate minimization problem. When used for regularizing the inverse problem $Ku=f$, the latter becomes

$$\min_u \frac{\|Ku-f\|_2^2}{2}+\mathrm{TGV}_\alpha^2(u) \qquad \text{with} \qquad \mathrm{TGV}_\alpha^2(u)=\min_w \alpha_1\|\nabla u-w\|_1+\alpha_0\|\varepsilon w\|_1$$

where u is the data to reconstruct, K an arbitrary linear forward mapping and f some given data. In the definition of TGV, α_0 and α_1 are the regularization parameters, ∇u denotes the derivative and $\varepsilon w=(\nabla w + \nabla w^T)/2$ is the symmetrized derivative. This minimization problem is convex and can be cast into a convex-concave saddle-point problem. Efficient abstract algorithms are available for the latter, here we choose the method of [4] in the variants described in [5] and a parallelized GPU implementation.

Results: To test the effectiveness of TGV^2-regularization, solutions for a deconvolution problem were computed [5]. A known image was blurred by convolving with an out-of-focus point-spread function. Noise was added such that direct inversion is no longer possible. Afterwards, deconvolution regularized with TGV^2 and TV was performed. The outcome of this experiment can be seen in Fig. 1. In comparison to TV, smooth regions corresponding to soft tissue are more faithfully recovered by TGV^2. In a second experiment, we performed reconstruction from parallel undersampled radial *k*-space data [3]. A known image was sampled, in *k*-space, with 24 radial spokes and 32 channels. Reconstruction was performed using the NUFFT and CGSENSE [6] methods as well as TGV^2-regularization, see Fig. 2. Again, the latter yields high-quality results.

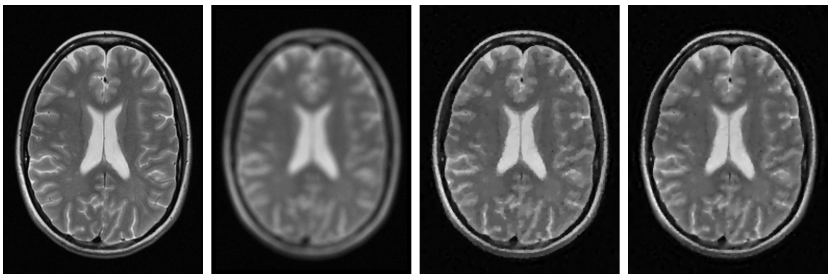

Fig. 1: Deconvolution example. From left to right: Ground truth, blurred and noisy data, TV-regularized reconstruction, TGV^2-regularized reconstruction.

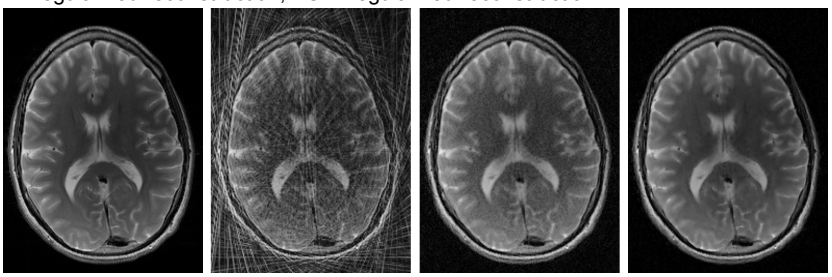

Fig. 2: Undersampling reconstruction example. From left to right: Ground truth, NUFFT reconstruction, CGSENSE reconstruction, TGV^2-regularized reconstruction.

Conclusion: TGV provides a flexible regularization framework for recovering piecewise smooth data, in particular images of biological tissue which are not piecewise constant. It can be applied to a wide range of inverse problems. Efficient GPU-based algorithms solving the associated minimization problems are available.

References: [1] Rudin et al. Nonlinear total variation based noise removal algorithm. Physica D 60:259-268 (1992). [2] Bredies et al. Total generalized variation. SIIMS 3:492-526 (2010). [3] Knoll et al. Second order total generalized variation (TGV) for MRI. MRM 65:480-491 (2011). [4] Chambolle and Pock. A first-order primal-dual algorithm for convex problems with applications to imaging. JMIV 40:120-145 (2011). [5] Bredies. Recovering piecewise smooth multichannel images by minimization of convex functionals with total generalized variation penalty. SFB-Report 2012-006 (2012). [6] Pruessmann et al. Advances in sensitivity encoding with arbitrary k-space trajectories. MRM 46:638-651 (2001).

Iron Mapping in Parkinson's Disease

W. R. Wayne Martin, MD
University of Alberta

Background/Purpose:
Parkinson's disease (PD) is a common neurodegenerative disorder that affects 2-3% of individuals over age 65. The major clinical features include a resting tremor, bradykinesia, rigidity and impaired postural reflexes while the underlying pathophysiology relates, at least in part, to a loss of dopaminergic neurons projecting from the substantia nigra pars compacta (SNc) to the striatum. The diagnosis is clinical, based on the presence of the characteristic neurological features. There are no confirmatory diagnostic tests although radionuclide imaging with PET or SPECT can provide evidence of impaired function in presynaptic dopaminergic nerve terminals. There is a need in clinical research for a technique that may provide diagnostic information as well as objective information regarding disease severity and progression. Several lines of evidence point to the possibility of increased iron content in the SNc in this disorder, raising the possibility that iron mapping with MRI may be a useful technique in this regard.

Methods:
We have explored the use of a multiple gradient echo sequence at 3 tesla designed for rapid single-scan mapping of the proton transverse relaxation rate (R2*) in untreated subjects with PD and in age-matched normal controls. Voxel-wise measurements of R2* were obtained from midbrain regions containing the SNc and from forebrain regions containing the striatum and pallidum. These measurements were correlated with clinical estimates of disease severity from the motor subsection of the Unified Parkinson's Disease Rating Scale.

Results:
Our results indicated a difference in measured R2* values between PD patients and controls in the lateral SNc, corresponding to the known distribution of neuronal loss occurring in this disorder. Linear regression indicated a correlation between the lateralized motor score from the clinically most affected side and R2* values from the opposite lateral SNc.

Discussion:
These preliminary results are consistent with the suggestion that increased nigral iron content demonstrated with high field MRI in PD may provide useful diagnostic information as well as an objective marker for disease progression. We are currently pursuing longitudinal studies with this methodology and are exploring other methods for mapping the iron-rich regions of the brain in PD and related neurodegenerative disorders. There are several caveats that must be kept in mind, however, in the interpretation of iron mapping in these disorders. Accurate localization of the SNc on midbrain images has been a substantial source of variability in reports of MRI in PD. The immediately adjacent substantia nigra pars reticulata has a higher iron content than does the SNc but does not contain the dopaminergic nigrostriatal neurons that are known to be involved in PD. The mechanism underlying the iron accumulation observed in PD remains uncertain. There is controversy regarding whether iron is actually pathogenic in this situation or whether it is merely an innocent bystander serving as a marker of neurodegeneration. Further studies are needed to help resolve these issues

References:
Wild JM, Martin WRW, Allen PS. A multiple gradient echo sequence optimized for rapid, single scan mapping of R2* at high B0. Magn Reson Med 2002;48:867-876

Martin WRW, Wieler M, Gee M. Midbrain iron content in early Parkinson disease: A potential biomarker of disease status. Neurology 2008;70;1411-1417

Applications of Short Echo QSM

[1,2]EM Haacke, PhD., [3]S Buch, MS, [3]S Liu, BS, [2]D Wu, [3]Y Ye, PhD, [3]J Neelavalli, PhD and [1]YCN Cheng, PhD
[1]Wayne State University, [2]The MRI Institute and [3]McMaster University

Introduction

Quantitative Susceptibility mapping (QSM) has its roots in phase imaging and in a sense was stimulated by the major research and clinical interest in susceptibility weighted imaging (SWI) [1–5]. Most of the applications of SWI have used long echo times to enhance susceptibility effects and small phase changes. However, there are practical problems with this long echo time (TE) approach, in terms of both macroscopic and microscopic (relative to pixel size) phase aliasing. The former can be corrected while the latter leads to T_2^* signal loss and the infamous blooming artifact that makes the object appear larger than its actual size. In turn, this leads to underestimates of susceptibility values for small objects. Data collected at short TE could be used to address this problem. As one example, we have produced susceptibility maps of the leg with improved quality. We have also developed an interleaved double TE SWI sequence for both short and long echo scans. This approach can provide the means to handle both low and high iron concentrations and better unwrap the phase data using a complex division method. The resulting complex divided images can then be used to make a more accurate forward model prediction of the geometry effects without the normally required phase unwrapping algorithms. This helps to preserve the local phase information, without the need for heavy high pass filters [6]. One of the more interesting aspects of using short TE is being able to handle the phase changes originating from areas or tissues with no MR signal, such as the air, bone and calcium. The susceptibility differences around such areas can be so large that the susceptibility cannot be reliably quantified unless a short enough TE is used.

Methods

QSM in the leg

For generating the QSM of the leg, we collected sagittal SWI data using a single echo SWI sequence with: TE=7.65msec (at which water and fat are roughly in phase), TR=20ms, FA=15°, B_0=3T (Siemens Verio) and $0.5\times0.5\times1mm^3$ resolution. The geometry of the leg was extracted from the magnitude images and was used to remove the air-tissue induced field variation by forward modeling. There was minimal phase aliasing after the geometry induced field was removed. The remnant phase aliasing was removed by locally shifting the baseline of the phase images (shifting the phase origin from zero toward $-\pi$ given the knowledge that all aliasing is occurring because the phase is increasing toward positive π and then aliasing). Then, 3D high-pass filtering was applied in the image domain, using a normalized spherical kernel with variable size (32 pixels for the central part of the leg and smoothly reduced to 4 pixels near the edge). In order to reduce the edge artifacts induced by the high-pass filtering, the phase values in the bone region were obtained through 3D interpolation prior to the high-pass filtering. QSM was generated using truncated k-space division with regularization threshold 0.1.

Sinus mapping

Removing background field effects and phase unwrapping are the first steps for any susceptibility mapping procedure. Hence, the main function of this step is to preserve the phase by avoiding using any filtering techniques, such as homodyne high pass (HP) filter, or if possible, other sophisticated approaches that require phase unwrapping. Using HP filter on the phase data can affect the accuracy of susceptibility quantification since it leads to loss of phase information.

When there is a large susceptibility difference, such as air/tissue interfaces, one of the best ways to reduce aliasing is simply to use a short echo. In the following discussion, we will focus on the use of a very short echo time of just 2.58ms for QSM.

In order to achieve this short TE, we have developed an interleaved double TE GRE sequence to simultaneously collect two images with arbitrary TE values. For each phase encoding step, two consecutive TR blocks were executed. The first TR block collects the data for the first image, and the echo time is TE_1, while the second TR

block collects the second image with echo time as TE_2. Otherwise the two TR blocks are identical. This sequence at each echo time is fully flow compensated. TE_1 and TE_2 can be set independently. By collecting two images in such an interleaved manner, the two images will be precisely realigned to each other, and this ensures that the only difference between the two images is their TE values.

As an example of this sinus mapping concept, we collected SWI data sagittally using the interleaved double echo sequence with: TE_1=5.68ms and TE_2=8.25ms, TR=20ms, FA=15°, B_0=3T and $0.5\times0.5\times2mm^3$ resolution acquired with an FOV that covers the whole brain and neck. The 5.68ms data were complex divided by the 8.25ms data to produce a new phase image with an effective TE of 2.58ms, which was selected to be close to the in-phase value of water and fat. This is important when we examine the signal from extra-cerebral region as there are fatty tissues in this region and any major chemical shift in the fat can be misconstrued as a susceptibility effect. Any linear phase shifts were removed by shifting the echo back to the center of k-space, and any remnant aliasing in the 2.58ms phase image was removed by shifting the baseline. Then we used a regularization threshold of 0.2 on the QSM results [1] to generate the susceptibility maps (SMs) of sinuses. Finally, to focus just on the sinuses, the SMs were thresholded by removing all values lower than 4ppm. What remains can be considered as the major components of the sinuses and can be used in any forward modeling to calculate and reduce the field induced by the sinuses by subtracting the estimated phase from the original phase.

Results

Intermediate echo time single echo approach: For the leg, with only one TE of 7.65ms, we were able to remove the background field induced by the complex geometry through forward modeling and variable high-pass filtering (Figure 1b). Note that the geometry induced field variation as indicated by the white arrows in Figure 1a is removed in Figure 1b. The edge regions are also handled properly. This leads to better quality of SMs (Figure 1c).

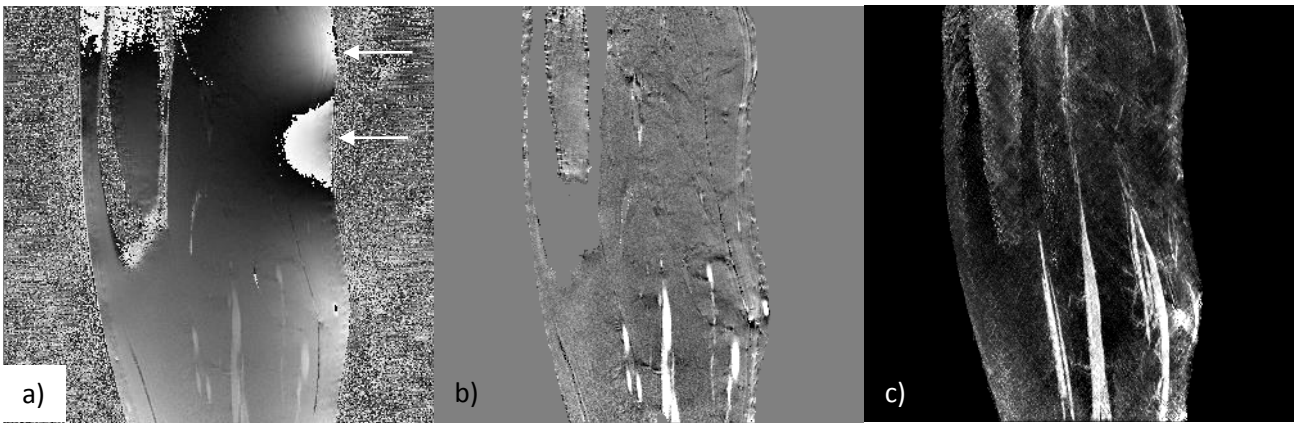

Figure 1. a) Original phase image, b) phase image after applications of forward modeling to remove some background phase and of the variable HP filter and c) the maximum intensity projection (MIP) of the susceptibility maps. The data were collected on the leg using TE=7.65ms.

Short TE two echo approach: Figure 2a demonstrates the complex division result of the brain with an effective echo time of 2.58ms. This image shows considerably less phase wraps around the air-tissue interfaces, making it possible to preserve the phase information even outside the brain (pericranium to scalp). In Figures 2b and 2c, the susceptibility values are negative in the bone regions, but more positive in the sinuses than other areas of the brain, as expected. With a better knowledge of the shape of the sinuses, one can better estimate the phase induced by the geometry of the susceptibility source itself (Figure 3) using the forward modeling [2]. After subtracting the estimated sinus phase from the original longer echo data (TE=8.25ms), a Homodyne high pass filter was applied. Figure 3 compares the phase image obtained from above described approach with the traditional HP filtered phase image, revealing the important local tissue signal hidden under the sinus phase.

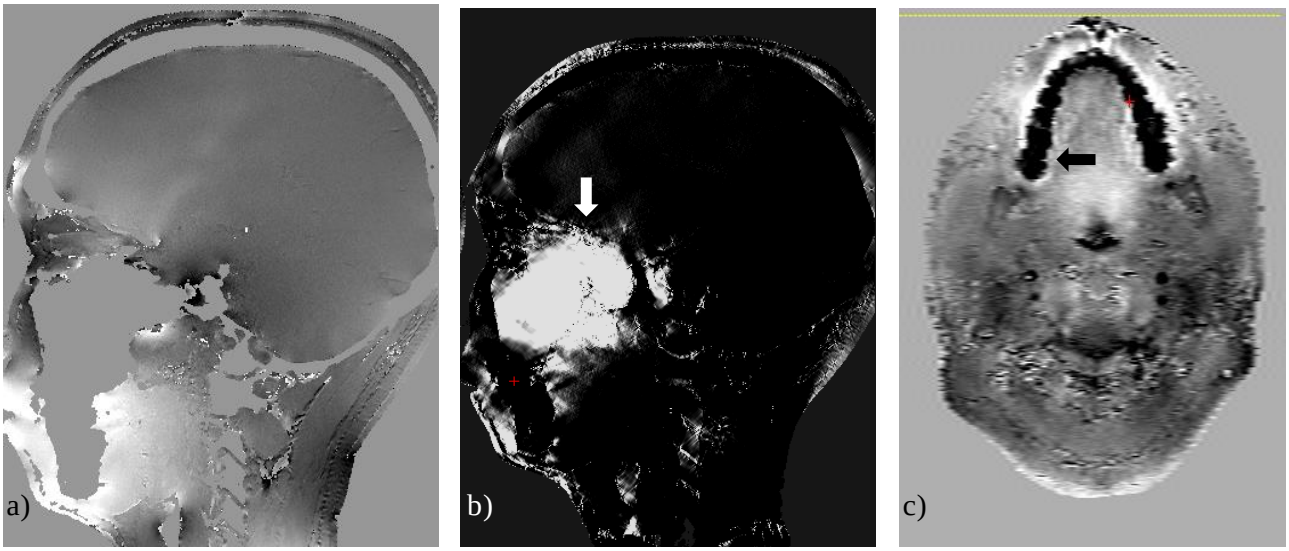

Figure 2. a) The resultant phase (TE=2.58ms) after complex division using TE=5.68ms and TE=8.25ms phase datasets. b) and c): SMs generated by preserving the phase inside the head (pericranium to scalp) in sagittal and transverse planes, respectively. The white arrow in b) points towards the reconstructed brain sinus and the black arrow in c) identifies the teeth.

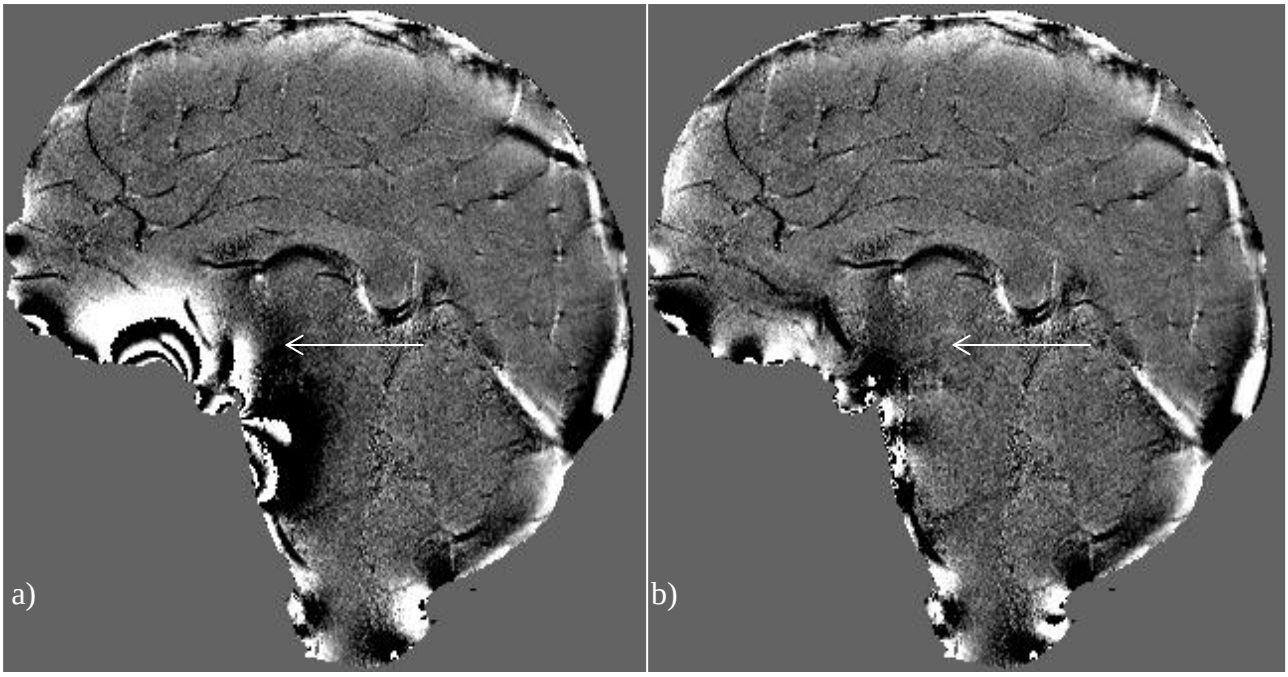

Figure 3. a) Traditional homodyne high-pass filtered (32x32) phase images, b) high pass filtered (32x32) phase image after subtracting the sinus phase simulated from forward modeling of the sinus geometry.

Discussion and Conclusion:

For many years, the focus of quantitative susceptibility mapping has been using long echo times (usually on the order of 20 to 30ms at 3T) to image brain iron, small veins and fiber tracts with different levels of myelin contents. The reasons are basically two-fold. First, one expects better SNR from phase images at longer echo times and second, if susceptibility differences are small (say on the order of 10 to 20 ppb) then it will need a long echo time to reveal these phase differences. However, there are a number of interesting studies that can be done with shorter echo times, for example, estimating oxygen saturation in major veins[7,8], vessel wall differences in the peripheral vasculature[9] or any other part of the body for that matter. Our earlier work showed that even an echo time of 7 to 8ms is enough to extract phase information with good SNR in imaging vessels in the leg[7–9] with much less aliasing than with the conventional approach of TE = 20ms.

It is understood that the shorter the echo time, the less the phase aliasing. This is especially true for areas with high susceptibility differences such as the air-tissue boundaries in the sinuses. These high susceptibility sources then create a major non-local problem of phase invading other regions of interest (for example, around the mid-brain). By using shorter and shorter echo times, regions which are usually heavily aliased, now have no need for phase unwrapping. The usual local contributions from the brain can now be treated as noise and *the major goal now becomes imaging the sinuses not imaging the brain.* By thresholding out those parts of the brain with tiny susceptibility effects, the remnant SMs will represent the air in the brain. A major point here is that unlike the original forward modeling approach that required estimating the region of the sinuses from the magnitude images, the resulting SMs of the sinuses will have the precise geometric information to recreate the complex and significant phase effects seen at long echo times, which can be thus estimated and subsequently removed. Nevertheless, the magnitude images can still be used as a constraint to keep only those points that are clearly air but not tissue. Finally, by using forward modeling of these detailed images of the sinuses, the deleterious sinus effects can be, to a large degree, removed from longer echo times. The success of this sinus mapping was made possible by keeping as much information from all tissues surrounding the sinuses.

The ability to map structures other than tissues with water using susceptibility mapping is possible as long as the object of interest has relatively uniform susceptibility and is surrounded by other structures with MR signal, provided that sufficient phase information is available to properly extract the local susceptibility. One of the key features of our approach is that the extra-cerebral tissues are included, and no brain extraction algorithm was used in this approach. It is critical to maintain the pristine phase around the sinuses as this provides valuable information for estimating the susceptibility of these air regions.

In conclusion, shorter echo times make it possible to image the surface of teeth, bone (making imaging the spine more interesting for QSM), and other structures with a large susceptibility but low or no MR signal. Instead of being viewed as sources of problems, now these structures can be viewed as an important source of information. Finally, one can imagine in the future using this concept to image many other structures. For example, this concept could be applied in material science for imaging solids or structures with inclusions where the difference in susceptibility will manifest in field changes outside the object, but there is no need for this structure to contain water.

References

1. Haacke, E. M., Tang, J., Neelavalli, J. & Cheng, Y. C. . Susceptibility mapping as a means to visualize veins and quantify oxygen saturation. *Journal of Magnetic Resonance Imaging* **32**, 663–676 (2010).
2. Haacke, E. M., Xu, Y., Cheng, Y. N. & Reichenbach, J. R. Susceptibility weighted imaging (SWI). *Magnetic Resonance in Medicine* **52**, 612–618 (2004).
3. Liu, J. *et al.* Morphology enabled dipole inversion for quantitative susceptibility mapping using structural consistency between the magnitude image and the susceptibility map. *Neuroimage* **59**, 2560–2568 (2012).
4. Schweser, F., Deistung, A., Lehr, B. W. & Reichenbach, J. R. Quantitative imaging of intrinsic magnetic tissue properties using MRI signal phase: An approach to in vivo brain iron metabolism? *NeuroImage* **54**, 2789–2807 (2011).
5. Liu, C. Susceptibility tensor imaging. *Magn Reson Med* **63**, 1471–1477 (2010).
6. Neelavalli, J., Cheng, Y. N., Jiang, J. & Haacke, E. M. Removing background phase variations in susceptibility-weighted imaging using a fast, forward-field calculation. *Journal of Magnetic Resonance Imaging* **29**, 937–948 (2009).
7. Barnes, S. & Haacke, E. M. Settling properties of venous blood demonstrated in the peripheral vasculature using susceptibility-weighted imaging (SWI). *J Magn Reson Imaging* **29**, 1465–1470 (2009).
8. Barnes, S. R. S. & Haacke, E. M. Susceptibility-weighted imaging: clinical angiographic applications. *Magn Reson Imaging Clin N Am* **17**, 47–61 (2009).
9. Yang, Q. *et al.* Imaging the vessel wall in major peripheral arteries using susceptibility-weighted imaging. *J Magn Reson Imaging* **30**, 357–365 (2009).

Inversion Algorithms: K-Space Based Approaches

Karin Shmueli
Department of Medical Physics and Bioengineering, University College London, United Kingdom

Background: Calculating susceptibility maps from MRI phase data is an inverse problem that can be simply expressed in the Fourier domain (k-space): $\chi(\boldsymbol{k}) = \frac{\Delta B_z(\boldsymbol{k})}{B_0}.D(\boldsymbol{k})^{-1}$ [Eq. 1] where $\chi(\boldsymbol{k})$ is the susceptibility distribution in k-space and $\Delta B_z(\boldsymbol{k})$ is the Fourier Transform (FT) of the measured z-component of the magnetic field perturbation and is scaled by the magnitude of the main magnetic field B_0. $D(\boldsymbol{k})$ is the FT of the unit dipole or convolution kernel that relates the field to the susceptibility in real space and is given by $D(\boldsymbol{k}) = \frac{1}{3} - \frac{k_z^2}{k^2}$ where k_z is the z-component of the k-space vector $\boldsymbol{k}$ whose magnitude is given by $k^2 = k_x^2 + k_y^2 + k_z^2$. This inverse problem is ill-posed, meaning that a unique solution does not exist because $\chi(\boldsymbol{k})$ tends to infinity where $D(\boldsymbol{k})=0$ on two conical surfaces in k-space at the magic angle to B_0. The problem is also ill-conditioned, meaning that noise or errors in $\Delta B_z(\boldsymbol{k})$ close to these conical surfaces are amplified. "K-space based" algorithms overcome the ill-posed and ill-conditioned nature of the inverse problem by removing, substituting or correcting the data in the ill-conditioned regions **R** on and near these cones in k-space.

Methods: Such k-space based algorithms also do not usually involve introducing spatial (image-space) prior information to solve the inverse problem i.e. regularization. To some extent, the inversion approach is determined by the MRI acquisition parameters. For example, if the field is measured with the object ($\chi(\boldsymbol{k})$) at multiple (≥ 3) angles to B_0 [**1-3**] then **R** can simply be filled with data acquired at the other orientations and $\chi(\boldsymbol{k})$ outside **R** is averaged over orientations. Most multi-angle methods rely on iterative least-squares fitting done in image space. Due to the practical difficulty of multi-angle acquisitions, several methods have been developed for single-angle acquisitions. These can be classified according to 1) **R**: which regions of k-space data are modified and 2) the modification technique. Perhaps the simplest inversion algorithms are those involving thresholded k-space division (TKD) in which the extent of **R** is determined by a threshold applied $D(\boldsymbol{k})^{-1}$ [**4**] or $D(\boldsymbol{k})$ [**3, 5-8**] and 2) have included truncation of $|D(\boldsymbol{k})^{-1}|$ above a certain value [**4**], masking out ill-conditioned data [**3, 6**], or combining these by ensuring $|D(\boldsymbol{k})^{-1}|$ transitions smoothly between its maximum values and zero on the k-space cones [**5**]. $\chi(\boldsymbol{k})$ inside **R** has also been obtained by solving the derivative of Eq. 1 with respect to k_z [**7**] and using compressed sensing [**8**]. Some inversion approaches can be considered as hybrid algorithms alternating between k-space and image-space [**9**]. Even some regularization-based approaches [**10**] rely on first subdividing k-space into three sub-domains (including **R**) and using different inversion techniques for each.

Results and Discussion: Each of these algorithms has relative merits and disadvantages. Multi-angle approaches, although for a time considered a gold-standard, have the drawback of averaging out the orientation dependence of the measured susceptibility [**11, 12**]. Although they can suffer from streaking artifacts, single-angle k-space-based approaches such as TKD are straightforward and computationally efficient relative to regularization or image-space-based methods that may result in a smoothed $\chi(\mathbf{r})$ affected by the spatial prior information used [**2**]. With TKD methods, there is a trade-off in choosing **R** large enough to reduce noise and sufficiently small to preserve spatial resolution and contrast.

Conclusion: Formulating the inverse problem in k-space is an important framework useful for understanding the plethora of different inversion algorithms. The classification into k-space or image-space based approaches is blurred by newer hybrid algorithms [**9, 10**] that exploit the advantages of both types of method.

References: **1.** T. Liu, et al., *Magn Reson Med*, 2009. 61(1): 196-204. **2.** S. Wharton and R. Bowtell, *Neuroimage*, 2010. 53(2): 515-25. **3.** S. Wharton, et al., *Magn Reson Med*, 2010. 63(5): 1292-304. **4.** K. Shmueli, et al., *Magn Reson Med*, 2009. 62(6): 1510-22. **5.** E.M. Haacke, et al., *Journal of Magnetic Resonance Imaging*, 2010. 32(3): 663-676. **6.** G. Grabner, et al., *Journal of Magnetic Resonance Imaging*, 2010. 32(2): 289-297. **7.** W. Li, et al., *Neuroimage*, 2011. 55(4): 1645-1656. **8.** B. Wu, et al., *Magnetic Resonance in Medicine*, 2012. 67(1): 137-147. **9.** J. Tang, et al., *Magn Reson Med*, 2013. 69(5): 1396-407. **10.** F. Schweser, et al., *Neuroimage*, 2012. 62(3): 2083-2100. **11.** J. Lee, et al., *Proc Natl Acad Sci U S A*, 2010. 107(11): 5130-5. **12.** C. Liu, *Magn Reson Med*, 2010. 63(6): 1471-7.